

A Manifold Perspective on the Statistical Generalization of Graph Neural Networks

Zhiyang Wang*, Juan Cerviño[†], Alejandro Ribeiro*
zhiyangw@seas.upenn.edu, jcervino@mit.edu, aribeiro@seas.upenn.edu

*University of Pennsylvania, [†]Massachusetts Institute of Technology

Abstract

Graph Neural Networks (GNNs) extend convolutional neural networks to operate on graphs. Despite their impressive performances in various graph learning tasks, the theoretical understanding of their generalization capability is still lacking. Previous GNN generalization bounds ignore the underlying graph structures, often leading to bounds that increase with the number of nodes – a behavior contrary to the one experienced in practice. In this paper, we take a manifold perspective to establish the statistical generalization theory of GNNs on graphs sampled from a manifold in the spectral domain. As demonstrated empirically, we prove that the generalization bounds of GNNs decrease linearly with the size of the graphs in the logarithmic scale, and increase linearly with the spectral continuity constants of the filter functions. Notably, our theory explains both node-level and graph-level tasks. Our result has two implications: i) guaranteeing the generalization of GNNs to unseen data over manifolds; ii) providing insights into the practical design of GNNs, i.e., restrictions on the discriminability of GNNs are necessary to obtain a better generalization performance. We demonstrate our generalization bounds of GNNs using synthetic and multiple real-world datasets.

Introduction

Graph convolutional neural networks (GNNs) (Scarselli et al., 2008; Defferrard et al., 2016; Bruna et al., 2013) have emerged as one of the leading tools for processing graph-structured data. There is abundant evidence of their empirical success across various fields, including but not limited to weather prediction (Lam et al., 2023), protein structure prediction in biochemistry (Jumper et al., 2021; Strokach et al., 2020), resource allocation in wireless communications (Wang et al., 2022a), social network analysis in sociology (Fan et al., 2020), point cloud in 3D model reconstruction (Shi & Rajkumar, 2020) and learning simulators (Fortunato et al., 2022).

The effectiveness of GNNs relies on their empirical ability to *predict* over unseen data. This capability is evaluated theoretically with *statistical generalization* in deep learning theory (Kawaguchi et al., 2017), which quantifies the difference between the *empirical risk* (i.e. training error) and the *statistical risk* (i.e. testing error). Despite the abundant evidence of GNNs’ generalization capabilities in practice, developing concrete theories to explain their generalization is an active area of research. Many recent works have studied the generalization bounds of GNNs without any dependence on the underlying model responsible for generating the graph data (Scarselli et al., 2018; Garg et al., 2020; Verma & Zhang, 2019). Generalization analysis on graph classification, when graphs are drawn from random limit models, is also studied in a series of works (Ruiz et al., 2023; Maskey et al., 2022, 2024; Levie, 2024). In this work, we take the manifold perspective to formulate graph data on continuous topological spaces, i.e., manifolds. We emphasize that manifolds are realistic models to generate graph data that enable rigorous theoretical analysis and a deep understanding of the behaviors of GNNs.

We explore the generalization bound of GNNs through the lens of manifold theory on both node-level and graph-level tasks in the spectral domain. The graphs are constructed based on points randomly sampled from underlying manifolds, indicating that the manifold can be viewed as a statistical model for these discretely sampled points. As convolutional neural network architectures have been established over manifolds (Wang et al., 2022b), the convergence of GNNs to manifold neural networks (MNNs) and the algebraical equivalence of these two frameworks facilitate a detailed generalization understanding of GNNs through spectral analysis. We demonstrate that, with an appropriate graph construction based on the sampled points from the manifold, the generalization gap between empirical and statistical risks decreases with the number of sampled points in the graphs (Figure 1c) on both node-level and graph-level tasks. More importantly, the generalization gap increases

linearly with the continuity constants of frequency response functions of graph filters composing the GNN (Figure 1d). We observe that with low-pass and spectral continuous filters, the GNNs are generalizable across different nodes or graphs generated from the same underlying manifold. This provides insight into the practical graph filter design from a spectral perspective. Moreover, the theoretical results indicate a trade-off between the discriminability and generalization capability of GNNs, suggesting that restrictions on the discriminability of GNNs are necessary to maintain generalization performance.

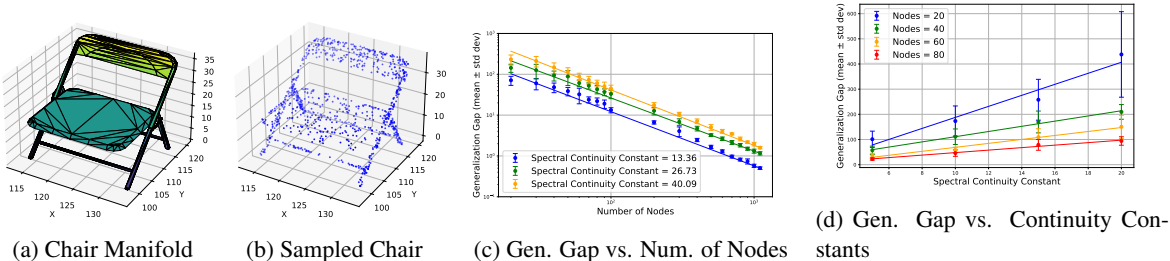


Figure 1: Synthetic experimental results are shown on the uniformly sampled chair manifold. We construct a graph with different numbers of nodes, fix the weights of a GNN, and compute the generalization gap. We construct the graph by computing the edges for nodes that are ϵ close (cf. (3)). In Figure 1c we fix the spectral continuity constant (see Definition 4) and vary the number of nodes. As our theory predicts, we see that a smaller spectral continuity constant translates into a smaller generalization gap – as the blue line is below the green line which is below the orange line. In Figure 1d we fix the number of nodes in the graph and vary the spectral continuity constant in the GNN. For the same number of nodes, a larger spectral continuity constant translates into a larger generalization gap.

We introduce a novel unified analysis of the generalization of GNNs to unseen nodes and graphs, by relating the GNNs with MNNs in the spectral domain. We further propose restrictions on the discriminability of GNNs from the spectral perspective which results from assumptions on the continuity of the filter frequency response functions. We provide extensive experiments both on synthetic and real-world datasets to verify our generalization conclusions. Our contribution is four-fold:

1. We prove the generalization bound of GNNs on graphs generated from an underlying manifold on both node-level (Theorem 1) and graph-level (Theorem 2) by relating the algebraically equivalent GNNs and MNN in the spectral domain.
2. We provide novel generalization gap bounds that decrease linearly with the nodes of the graph in the logarithmic scale, and increase linearly with the spectral continuity constants (Definition 4) of the filter functions.
3. We uncover an important trade-off between the discriminability and the generalization gap of GNNs, which guides practical GNN designs.
4. We verify the dependence of our generalization gaps on parameters, especially the continuity parameter, with a synthetic dataset – chair manifold – and eight real-world datasets – ArXiv, Citeseer, etc.

Related works

Generalization bounds of GNNs

Node level tasks We first give a brief recap of the generalization bounds of GNNs on node level tasks. In (Scarselli et al., 2018), the authors give a generalization bound of GNNs with a Vapnik–Chervonenkis dimension of GNNs. The authors in (Verma & Zhang, 2019) analyze the generalization of a single-layer GNN based on stability analysis, which is further extended to a multi-layer GNN in (Zhou & Wang, 2021). In (Ma et al., 2021), the authors give a novel PAC-Bayesian analysis on the generalization bound of GNNs across arbitrary subgroups of training and testing datasets. The authors derive generalization bounds for GNNs via transductive uniform stability and transductive Rademacher complexity in (Esser et al., 2021; Cong et al., 2021; Tang & Liu, 2023). The authors in (Yehudai et al., 2021) propose a size generalization analysis of GNNs correlated to the

discrepancy between local distributions of graphs. Different from these works, we consider a continuous manifold model when generating the graph data, which is theoretically powerful and realistic when characterizing real-world data. Furthermore, the generalization bounds proved in these works either grow with the size of the graph (Esser et al., 2021; Tang & Liu, 2023; Scarselli et al., 2018), with the node degree of the graphs (Cong et al., 2021) or the maximum eigenvalues of the graph (Verma & Zhang, 2019). Notably, our generalization bound decreases with the size of the graph given that it depends on the spectral properties of the filter functions over the manifold.

Graph level tasks There are also related works on the generalization analysis of GNNs on graph-level tasks. In (Garg et al., 2020), the authors form the generalization bound via Rademacher complexity. The authors in (Liao et al., 2020) build a PAC-Bayes framework to analyze the generalization capabilities of graph convolutional networks (Kipf & Welling, 2016) and message-passing GNNs (Gilmer et al., 2017), based on which the authors in (Ju et al., 2023) improve the results and prove a lower bound. The bounds either grow with the number of nodes (Liao et al., 2020) or the degree of the graphs (Garg et al., 2020) while our bound decreases with the number of nodes in the graph given that it better approximates the underlying model – the manifold. The works in (Maskey et al., 2022, 2024; Levie, 2024) are most related to ours, which also consider the generalization of GNNs on a graph limit model, in their case a *graphon*. Different from our setting, the authors see the graph limit as a random continuous model. They study the generalization of graph classification problems with message-passing GNNs with graphs belonging to the same category sampled from a continuous limit model. The generalization bound grows with the model complexity and decreases with the number of nodes in the graph. We show that a GNN trained on a single graph sampled from each manifold is enough, and can generalize and classify unseen graphs sampled from the manifold set.

Neural networks on manifolds

Geometric deep learning has been proposed in (Bronstein et al., 2017) with neural network architectures raised in manifold space. The authors in (Monti et al., 2017) and (Chakraborty et al., 2020) provide neural network architectures for manifold-valued data. In (Wang et al., 2024b) and (Wang et al., 2022b), the authors define convolutional operation over manifolds and see the manifold convolution as a generalization of graph convolution, which establishes the limit of neural networks on large-scale graphs as manifold neural networks (MNNs). The authors in (Wang et al., 2024a) further establish the relationship between GNNs and MNNs with non-asymptotic convergence results for different graph constructions. Some studies have used graph samples to infer properties of the underlying manifold itself. These properties include the validity of the manifold assumption (Fefferman et al., 2016), the manifold dimension (Farahmand et al., 2007) and the complexity of these inferences (Narayanan & Niyogi, 2009; Aamari & Knop, 2021). Other research has focused on prediction and classification using manifolds and manifold data, proposing various algorithms and methods. Impressive examples include the Isomap algorithm (Choi & Choi, 2004; Wu & Chan, 2004; Yang et al., 2016a) and other manifold learning techniques (Talwalkar et al., 2008). These techniques aim to infer manifold properties without analyzing the generalization capabilities of GNNs operated on the sampled manifold.

Preliminaries

Graph neural networks

Setup An undirected graph $\mathbf{G} = (\mathcal{V}, \mathcal{E}, \mathcal{W})$ contains a node set \mathcal{V} with N nodes and an edge set $\mathcal{E} \subseteq \mathcal{V} \times \mathcal{V}$. The weight function $\mathcal{W} : \mathcal{E} \rightarrow \mathbb{R}$ assigns weight values to the edges. We define the Graph Laplacian $\mathbf{L} = \text{diag}(\mathbf{A}\mathbf{1}) - \mathbf{A}$ where $\mathbf{A} \in \mathbb{R}^{N \times N}$ is the adjacency matrix. Graph signals are defined as functions mapping nodes to a feature value $\mathbf{x} \in \mathbb{R}^N$.

Graph convolutions and frequency response A graph convolutional filter $\mathbf{h}_{\mathbf{G}}$ is composed of consecutive graph shifts by graph Laplacian, defined as $\mathbf{h}_{\mathbf{G}}(\mathbf{L})\mathbf{x} = \sum_{k=0}^{K-1} h_k \mathbf{L}^k \mathbf{x}$ with $\{h_k\}_{k=0}^{K-1}$ as filter parameters. We replace \mathbf{L} with eigendecomposition $\mathbf{L} = \mathbf{V}\mathbf{\Lambda}\mathbf{V}^H$, where \mathbf{V} is the eigenvector matrix and $\mathbf{\Lambda}$ is a diagonal matrix with eigenvalues $\{\lambda_{i,N}\}_{i=1}^N$ as the entries. The spectral representation of a graph filter is

$$\mathbf{V}^H \mathbf{h}_{\mathbf{G}}(\mathbf{L})\mathbf{x} = \sum_{k=1}^{K-1} h_k \mathbf{\Lambda}^k \mathbf{V}^H \mathbf{x} = \hat{h}(\mathbf{\Lambda}) \mathbf{V}^H \mathbf{x}. \quad (1)$$

This leads to a point-wise frequency response of the graph convolution as $\hat{h}(\lambda) = \sum_{k=0}^{K-1} h_k \lambda^k$.

Graph neural networks A graph neural network (GNN) is a layered architecture, where each layer consists of a bank of graph convolutional filters followed by a point-wise nonlinearity $\sigma : \mathbb{R} \rightarrow \mathbb{R}$. Specifically, the l -th layer of a GNN that produces F_l output features $\{\mathbf{x}_l^p\}_{p=1}^{F_l}$ with F_{l-1} input features $\{\mathbf{x}_{l-1}^q\}_{q=1}^{F_{l-1}}$ is written as

$$\mathbf{x}_l^p = \sigma \left(\sum_{q=1}^{F_{l-1}} \mathbf{h}_{\mathbf{G}}^{lpq}(\mathbf{L}) \mathbf{x}_{l-1}^q \right), \quad (2)$$

for each layer $l = 1, 2, \dots, L$. The graph filter $\mathbf{h}_{\mathbf{G}}^{lpq}(\mathbf{L})$ maps the q -th feature of layer $l-1$ to the p -th feature of layer l . We denote the GNN as a mapping $\Phi_{\mathbf{G}}(\mathbf{H}, \mathbf{L}, \mathbf{x})$, where $\mathbf{H} \in \mathcal{H} \subset \mathbb{R}^P$ denotes a set of the graph filter coefficients at all layers and \mathcal{H} denotes the set of all possible parameter sets.

Manifold neural networks

Setup We consider a d -dimensional compact, smooth and differentiable Riemannian submanifold \mathcal{M} embedded in \mathbb{R}^M with finite volume. This induces a Hausdorff probability measure μ over the manifold with density function $\rho : \mathcal{M} \rightarrow (0, \infty)$, assumed to be bounded as $0 < \rho_{min} \leq \rho(x) \leq \rho_{max} < \infty$ for all $x \in \mathcal{M}$. The manifold data supported on each point $x \in \mathcal{M}$ is defined by scalar functions $f : \mathcal{M} \rightarrow \mathbb{R}$ (Wang et al., 2024b). We use $L^2(\mathcal{M})$ to denote L^2 functions over \mathcal{M} with respect to measure μ . The manifold with probability density function ρ is equipped with a weighted Laplace operator (Grigor'yan, 2006), generalizing the Laplace-Beltrami operator as

$$\mathcal{L}_\rho f = -\frac{1}{2\rho} \operatorname{div}(\rho^2 \nabla f), \quad (3)$$

with div denoting the divergence operator of \mathcal{M} and ∇ denoting the gradient operator of \mathcal{M} (Bronstein et al., 2017; Gross & Meinrenken, 2023).

Manifold convolutions and frequency responses The manifold convolution operation is defined relying on the Laplace operator \mathcal{L}_ρ and on the heat diffusion process over the manifold (Wang et al., 2024b). For a function $f \in L^2(\mathcal{M})$ as the initial heat condition over \mathcal{M} , the heat condition diffused by a unit time step can be explicitly written as $e^{-\mathcal{L}_\rho} f$. A manifold convolutional filter (Wang et al., 2024b) can be defined in a diffuse-and-sum manner as

$$g(x) = \mathbf{h}(\mathcal{L}_\rho) f(x) = \sum_{k=0}^{K-1} h_k e^{-k\mathcal{L}_\rho} f(x), \quad (4)$$

with the k -th diffusion scaled with a filter parameter $h_k \in \mathbb{R}$. We consider the case in which the Laplace operator is self-adjoint with respect to the inner product defined in (23) and positive-semidefinite and the manifold \mathcal{M} is compact, in this case, \mathcal{L}_ρ has real, positive and discrete eigenvalues $\{\lambda_i\}_{i=1}^{\infty}$, written as $\mathcal{L}_\rho \phi_i = \lambda_i \phi_i$ where ϕ_i is the eigenfunction associated with eigenvalue λ_i . The eigenvalues are ordered in increasing order as $0 = \lambda_1 \leq \lambda_2 \leq \lambda_3 \leq \dots$, and the eigenfunctions are orthonormal and form an eigenbasis of $L^2(\mathcal{M})$. When mapping a manifold signal onto the eigenbasis $[\hat{f}]_i = \langle f, \phi_i \rangle_{\mathcal{M}} = \int_{\mathcal{M}} f(x) \phi_i(x) d\mu(x)$, the manifold convolution can be written in the spectral domain as

$$[\hat{g}]_i = \sum_{k=0}^{K-1} h_k e^{-k\lambda_i} [\hat{f}]_i. \quad (5)$$

Hence, the frequency response of manifold filter is given by $\hat{h}(\lambda) = \sum_{k=0}^{K-1} h_k e^{-k\lambda}$.

Manifold neural networks A manifold neural network (MNN) is constructed by cascading L layers, each of which contains a bank of manifold convolutional filters and a pointwise nonlinearity $\sigma : \mathbb{R} \rightarrow \mathbb{R}$. The output manifold function of each layer $l = 1, 2, \dots, L$ can be explicitly denoted as

$$f_l^p(x) = \sigma \left(\sum_{q=1}^{F_{l-1}} \mathbf{h}_l^{pq}(\mathcal{L}_\rho) f_{l-1}^q(x) \right), \quad (6)$$

where f_{l-1}^q , $1 \leq q \leq F_{l-1}$ is the q -th input feature from layer $l-1$ and f_l^p , $1 \leq p \leq F_l$ is the p -th output feature of layer l . We denote MNN as a mapping $\Phi(\mathbf{H}, \mathcal{L}_\rho, f)$, where $\mathbf{H} \in \mathcal{H} \subset \mathbb{R}^P$ is a collective set of filter parameters in all the manifold convolutional filters.

Generalization analysis of GNNs based on manifolds

We consider a manifold \mathcal{M} as defined in Section , with a weighted Laplace operator \mathcal{L}_ρ as defined in (3). Since functions $f \in L^2(\mathcal{M})$ characterize information over manifold \mathcal{M} , we restrict our analysis to a finite-dimensional subset of $L^2(\mathcal{M})$ up to some eigenvalue of \mathcal{L}_ρ , defined as a bandlimited signal.

Definition 1. A manifold signal $f \in L^2(\mathcal{M})$ is bandlimited if there exists some $\lambda > 0$ such that for all eigenpairs $\{\lambda_i, \phi_i\}_{i=1}^\infty$ of the weighted Laplacian \mathcal{L}_ρ when $\lambda_i > \lambda$, we have $\langle f, \phi_i \rangle_{\mathcal{M}} = 0$.

Suppose we are given a set of N i.i.d. randomly sampled points $X_N = \{x_i\}_{i=1}^N$ over \mathcal{M} , with $x_i \in \mathcal{M}$ sampled according to measure μ . We construct a graph $\mathbf{G}(\mathcal{V}, \mathcal{E}, \mathcal{W})$ on these N sampled points X_N , where each point x_i is a vertex of graph \mathbf{G} , i.e. $\mathcal{V} = X_N$. Each pair of vertices (x_i, x_j) is connected with an edge while the weight attached to the edge $\mathcal{W}(x_i, x_j)$ is determined by a kernel function K_ϵ . The kernel function is decided by the Euclidean distance $\|x_i - x_j\|$ between these two points. The graph Laplacian denoted as \mathbf{L}_N can be calculated based on the weight function (Merris, 1995). The constructed graph Laplacian with an appropriate kernel function has been proved to approximate the Laplace operator \mathcal{L}_ρ of \mathcal{M} (Calder & Trillos, 2022; Belkin & Niyogi, 2008; Dunson et al., 2021). We present the following two definitions of K_ϵ .

Definition 2 (Gaussian kernel based graph (Belkin & Niyogi, 2008)). The graph $\mathbf{G}(X_N, \mathcal{E}, \mathcal{W})$ can be constructed as a dense graph degree when the kernel function is defined as

$$\mathcal{W}(x_i, x_j) = K_\epsilon \left(\frac{\|x_i - x_j\|^2}{\epsilon} \right) = \frac{1}{N} \frac{1}{\epsilon^{d/2+1} (4\pi)^{d/2}} e^{-\frac{\|x_i - x_j\|^2}{4\epsilon}}, \quad (x_i, x_j) \in \mathcal{E}. \quad (7)$$

The weight function of a Gaussian kernel based graph is defined on unbounded support (i.e. $[0, \infty)$), which connects x_i and x_j regardless of the distance between them. This results in a dense graph with N^2 edges. In particular, this Gaussian kernel based graph has been widely used to define the weight value function due to the good approximation properties of the corresponding graph Laplacians to the manifold Laplace operator (Dunson et al., 2021; Belkin & Niyogi, 2008; Xie et al., 2013).

Definition 3 (ϵ -graph (Calder & Trillos, 2022)). The graph $\mathbf{G}(X_N, \mathcal{E}, \mathcal{W})$ can be constructed as an ϵ -graph with the kernel function defined as

$$\mathcal{W}(x_i, x_j) = K_\epsilon \left(\frac{\|x_i - x_j\|^2}{\epsilon} \right) = \frac{1}{N} \frac{d+2}{\epsilon^{d/2+1} \alpha_d} \mathbb{1}_{[0,1]} \left(\frac{\|x_i - x_j\|^2}{\epsilon} \right), \quad (x_i, x_j) \in \mathcal{E}, \quad (8)$$

where α_d is the volume of a unit ball of dimension d and $\mathbb{1}$ is the characteristic function.

The weight function of an ϵ -graph is defined on a bounded support, i.e., only nodes that are within a certain distance of one another can be connected by an edge. It has also been shown to provide a good approximation of the manifold Laplace operator (Calder & Trillos, 2022). Figure 2 gives an illustration of both Gaussian kernel based graphs and ϵ -graphs sampled from point cloud models Wu et al. (2015).

Manifold label prediction via node label prediction

Suppose we have an input manifold signal $f \in L^2(\mathcal{M})$ and a label (i.e. target) manifold signal $g \in L^2(\mathcal{M})$ over \mathcal{M} . With an MNN $\Phi(\mathbf{H}, \mathcal{L}_\rho, \cdot)$, we predict the target value $g(x)$ based on input $f(x)$ at each point $x \in \mathcal{M}$. By sampling N points X_N over this manifold, we can approximate this problem in a discrete graph domain. Consider a graph $\mathbf{G}(X_N, \mathcal{E}, \mathcal{W})$ constructed with X_N as either a Gaussian kernel based graph (Definition 2) or an ϵ -graph (Definition 3) equipped with the graph Laplacian \mathbf{L}_N . Suppose we are given graph signal $\{\mathbf{x}, \mathbf{y}\}$ sampled from $\{f, g\}$ to train a GNN $\Phi_{\mathbf{G}}(\mathbf{H}, \mathbf{L}_N, \cdot)$, explicitly written as

$$[\mathbf{x}]_i = f(x_i), \quad [\mathbf{y}]_i = g(x_i) \quad \text{for all } x_i \in X_N. \quad (9)$$

We assume that the filters in MNN $\Phi(\mathbf{H}, \mathcal{L}_\rho, \cdot)$ and GNN $\Phi_{\mathbf{G}}(\mathbf{H}, \mathbf{L}_N, \cdot)$ are low-pass filters, which are defined explicitly as follows.

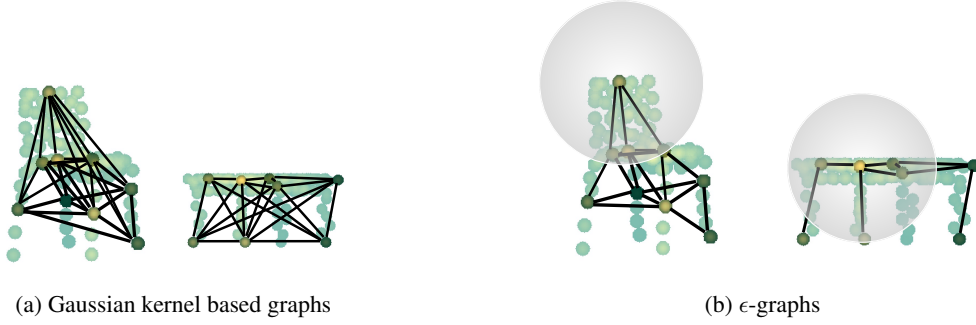


Figure 2: Illustration of the constructed graphs on points sampled over a chair and a table model.

Definition 4. A filter is a low-pass filter if its frequency response function satisfies

$$|\hat{h}(\lambda)| = \mathcal{O}(\lambda^{-d}), \quad |\hat{h}'(\lambda)| \leq C_L \lambda^{-d-1}, \quad \lambda \in (0, \infty), \quad (10)$$

with C_L a spectral continuity constant that regularizes the smoothness of the filter function.

To introduce the first of our two main results, we require introducing two assumptions.

AS 1. (Normalized Lipschitz nonlinearity) The nonlinearity σ is normalized Lipschitz continuous, i.e., $|\sigma(a) - \sigma(b)| \leq |a - b|$, with $\sigma(0) = 0$.

AS 2. (Normalized Lipschitz loss function) The loss function ℓ is normalized Lipschitz continuous, i.e., $|\ell(y_i, y) - \ell(y_j, y)| \leq |y_i - y_j|$, with $\ell(y, y) = 0$.

Assumption 1 is satisfied by most activations used in practice such as ReLU, modulus and sigmoid.

The generalization gap is evaluated between the *empirical risk* over the discrete graph model and the *statistical risk* over manifold model, with the manifold model viewed as a statistical model since the expectation of the sampled point is with respect to the measure μ over the manifold. The empirical risk over the sampled graph that we trained to minimize is therefore defined as

$$R_{\mathbf{G}}(\mathbf{H}) = \frac{1}{N} \sum_{i=1}^N \ell([\Phi_{\mathbf{G}}(\mathbf{H}, \mathbf{L}_N, \mathbf{x})]_i, [\mathbf{y}]_i). \quad (11)$$

The statistical risk over the manifold is defined as

$$R_{\mathcal{M}}(\mathbf{H}) = \int_{\mathcal{M}} \ell(\Phi(\mathbf{H}, \mathcal{L}_\rho, f)(x), g(x)) \mathrm{d}\mu(x). \quad (12)$$

The generalization gap is defined to be

$$GA = \sup_{\mathbf{H} \in \mathcal{H}} |R_{\mathcal{M}}(\mathbf{H}) - R_{\mathbf{G}}(\mathbf{H})|. \quad (13)$$

Theorem 1. Suppose the GNN and MNN with low-pass filters (Definition 4) have L layers with F features in each layer and the input signal is bandlimited (Definition 1). Under Assumptions 1 and 2 it holds in probability at least $1 - \delta$ that

$$GA \leq LF^{L-1} \left((C_1 C_L + C_2) \frac{\epsilon}{\sqrt{N}} + \frac{\pi^2 \sqrt{\log(1/\delta)}}{6N} \right) + F^L C_3 \left(\frac{\log N}{N} \right)^{\frac{1}{d}}, \quad (14)$$

with C_1 , C_2 , and C_3 depending on the geometry of \mathcal{M} , C_L is the spectral continuity constant in Definition 4.

1. When the graph is constructed with a Gaussian kernel (7), then $\epsilon \sim \left(\frac{\log(C/\delta)}{N} \right)^{\frac{1}{d+4}}$.
2. When the graph is constructed as an ϵ -graph as (8), then $\epsilon \sim \left(\frac{\log(CN/\delta)}{N} \right)^{\frac{1}{d+4}}$.

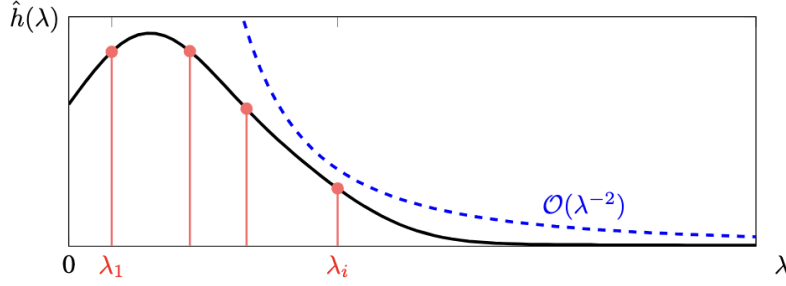


Figure 3: The x -axis stands for the spectrum, with each sample representing an eigenvalue. The black line illustrates a low-pass filter with red lines initiating the frequency responses of a filter on a given manifold. The blue dotted line shows the upper bound of the frequency response in Definition 4.

Proof. See Appendix for proof and the definitions of C_1 , C_2 and C_3 . \square

Theorem 1 shows that the generalization gap decreases approximately linearly with the number of nodes N in the logarithmic scale and that it also increases with the dimension of the underlying manifold d . Another observation is that the generalization gap scales with the size of the GNN architecture. Most importantly, we note the bound increases linearly with the spectral continuity constant C_L (Definition 4) – a smaller C_L leads to a smaller generalization gap bound, and thus a better generalization capability. While a smaller C_L leads to a smoother GNN, it discriminates fewer spectral components and, therefore, possesses worse discriminability. Consequently, we may observe a larger training loss with these smooth filters, presenting a trade-off between generalization and discriminative capabilities. Since the testing loss can be upper bounded by the sum of training loss and the bound of generalization gap, on a smoother GNN (a smaller C_L), the performance on the training data will be closer to the performance on unseen testing data. Therefore, having a GNN with a smaller spectral continuity constant C_L can guarantee more generalizable performance over unseen data from the same manifold. This also indicates that similar testing performance can be achieved by either a GNN with smaller training loss and worse generalization or a GNN with larger training loss and better generalization. In all, this indicates that there exists an optimal point to take the best advantage of the trade-off between a smaller generalization gap and better discriminability, resulting in a smaller testing loss decided by the spectral continuity constant of the GNN.

Manifold classification via graph classification

Suppose we have a set of manifolds $\{\mathcal{M}_k\}_{k=1}^K$, each of which is d_k -dimensional, smooth, compact, differentiable and embedded in \mathbb{R}^M with measure μ_k . Each manifold \mathcal{M}_k equipped with a weighted Laplace operator $\mathcal{L}_{\rho,k}$ is labeled with $y_k \in \mathbb{R}$. We assume to have access to N_k randomly sampled points according to measure μ_k over each manifold \mathcal{M}_k and construct K graphs $\{\mathbf{G}_k\}_{k=1}^K$ with graph Laplacians $\mathbf{L}_{N,k}$. The GNN $\Phi_{\mathbf{G}}(\mathbf{H}, \mathbf{L}_{N,\cdot}, \mathbf{x})$ is trained on this set of graphs with \mathbf{x}_k as the input graph signal sampled from the manifold signal $f_k \in L^2(\mathcal{M}_k)$ and $y_k \in \mathbb{R}$ as the scalar target label. The final output of the GNN is set to be the average of the output signal values on each node while the output of MNN $\Phi(\mathbf{H}, \mathcal{L}_{\rho,\cdot}, f)$ is the statistical average value of the output signal over the manifold. A loss function ℓ evaluates the difference between the output of GNN and MNN with the target label. The empirical risk of the GNN is

$$R_{\mathbf{G}}(\mathbf{H}) = \sum_{k=1}^K \ell \left(\frac{1}{N_k} \sum_{i=1}^{N_k} [\Phi(\mathbf{H}, \mathbf{L}_{N,k}, \mathbf{x}_k)]_i, y_k \right). \quad (15)$$

While the output of MNN is the average value over the manifold, the statistical risk is defined based on the loss evaluated between the MNN output and the label as

$$R_{\mathcal{M}}(\mathbf{H}) = \sum_{k=1}^K \ell \left(\int_{\mathcal{M}_k} \Phi(\mathbf{H}, \mathcal{L}_{\rho,k}, f_k)(x) d\mu_k(x), y_k \right). \quad (16)$$

The generalization gap is therefore

$$GA = \sup_{\mathbf{H} \in \mathcal{H}} |R_{\mathcal{M}}(\mathbf{H}) - R_{\mathbf{G}}(\mathbf{H})|. \quad (17)$$

Theorem 2. *Suppose the GNN and MNN with low-pass filters (Definition 4) have L layers with F features in each layer and the input signal is bandlimited (Definition 1). Under Assumptions 1 and 2 it holds in probability at least $1 - \delta$ that*

$$GA \leq LF^{L-1} \sum_{k=1}^K (C_1 C_L + C_2) \left(\frac{\epsilon}{\sqrt{N_k}} + \frac{\pi^2 \sqrt{\log(1/\delta)}}{6N_k} \right) + F^L C_3 \sum_{k=1}^K \left(\frac{\log N_k}{N_k} \right)^{\frac{1}{d_k}}, \quad (18)$$

with C_1 , C_2 , and C_3 depending on the geometry of \mathcal{M} , C_L is the spectral continuity constant in Definition 4.

1. When the graph is constructed with a Gaussian kernel (7), then $\epsilon \sim \left(\frac{\log(C/\delta)}{N_k} \right)^{\frac{1}{d_k+4}}$.
2. When the graph is constructed as an ϵ -graph as (8), then $\epsilon \sim \left(\frac{\log(CN_k/\delta)}{N_k} \right)^{\frac{1}{d_k+4}}$.

Proof. See Appendix for proof and the definitions of C_1 , C_2 and C_3 . □

Theorem 2 shows that a single graph sampled from the underlying manifold with large enough sampled points N_k from each manifold \mathcal{M}_k can provide an effective approximation to classify the manifold itself. The generalization gap also attests that the trained GNN can generalize to classify other unseen graphs sampled from the same manifold. Similar to the generalization result in node-level tasks, the generalization gap decreases with the number of points sampled over each manifold while increasing with the manifold dimension. A higher dimensional manifold, i.e. higher complexity, needs more samples to guarantee the generalization. The generalization gap also shows a trade-off between the generalization and discriminability as the bound increases linearly with the spectral continuity constant C_L . That is, to guarantee that a GNN for graph classification can generalize effectively, we must impose restrictions on the continuity of its filter functions, which in turn limits the filters' ability to discriminate between different graph features.

Experiments

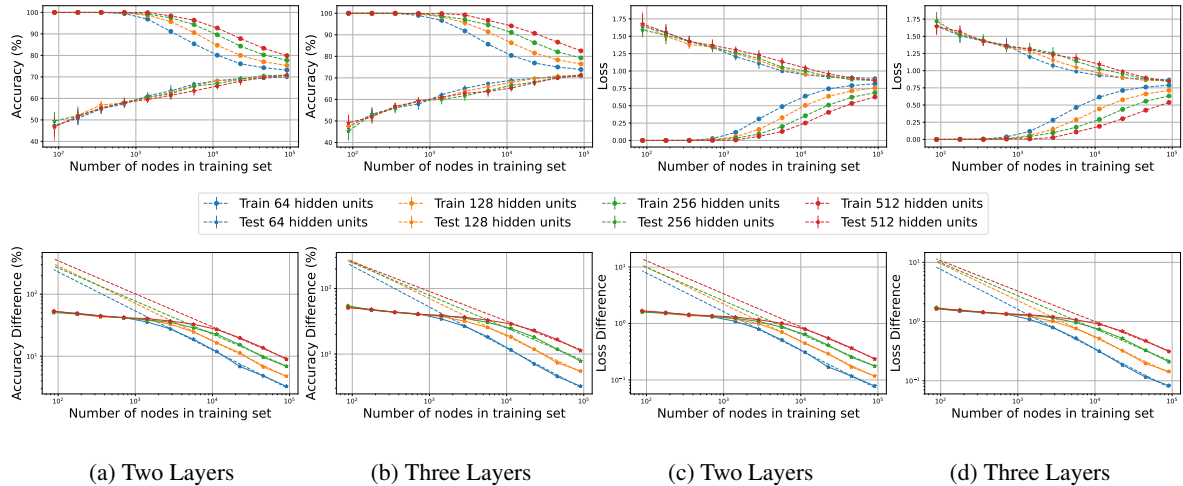


Figure 4: In the top row, we plot the difference in the accuracy and loss for columns 4a, 4b and 4c, 4d, respectively. On the bottom row, we plot the actual train and test values of the accuracy (4a, 4b), and the loss (4c, 4d). The plots are for the Arxiv dataset and $\{64, 128, 256, 512\}$ hidden units. For the bottom row, we also calculate the linear fit for the values whose training accuracy is below 95%, showing that our linear bound on the logarithm of the generalization gap for the logarithm of the number of nodes shares the same rate shown in Theorem 1.

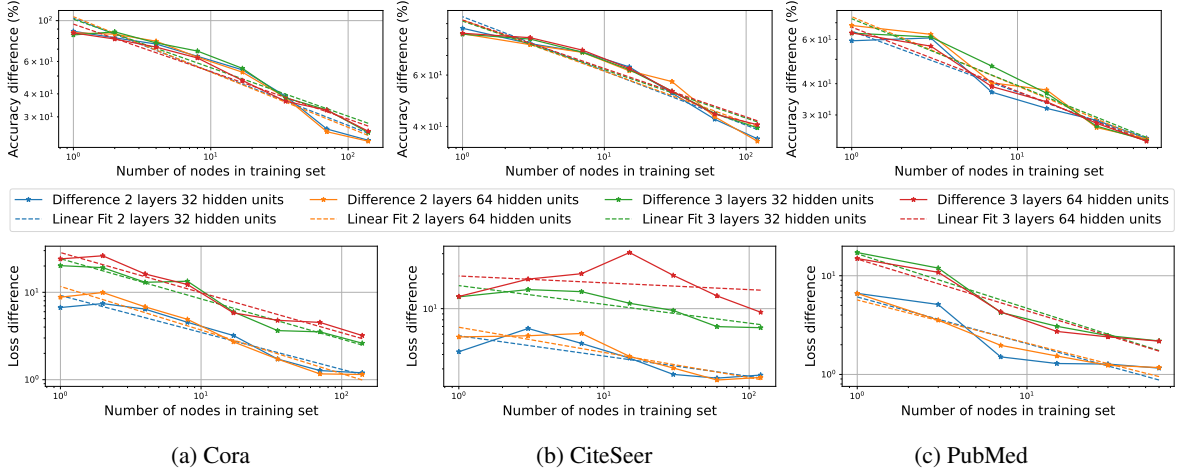


Figure 5: Generalization gap as a function of the number of nodes in the training set for accuracy (top) and loss (bottom) for the Cora, CiteSeer, and PubMed datasets.

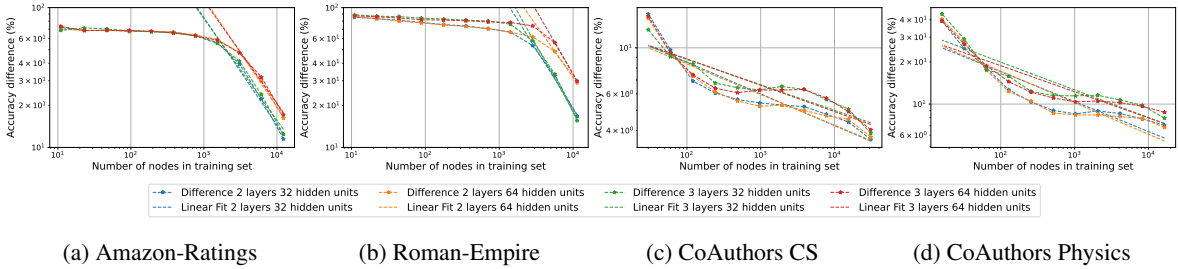


Figure 6: Accuracy generalization gap as a function of the number of nodes in the training set for the Amazon-Ratings, Roman-Empire, CoAuthors CS, and CoAuthors Physics datasets.

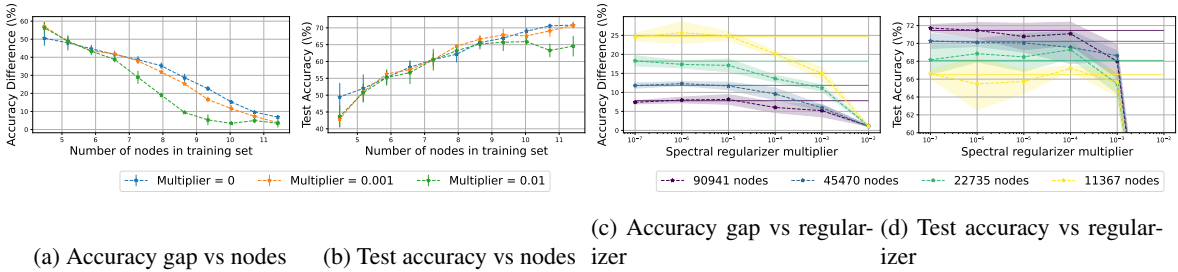
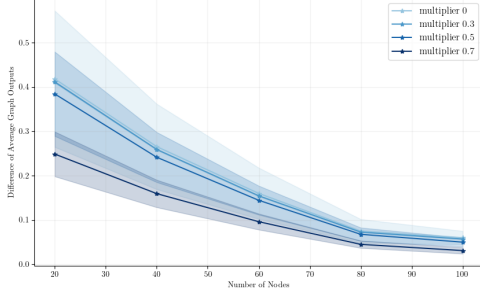


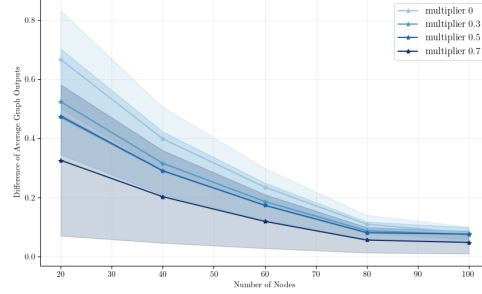
Figure 7: Spectral continuity constant effect on generalization gap and test accuracy.

In this Section, we evaluate the claims that we put forward empirically. We study the generalization gap (Theorems 1 and 2) bound on several node classification and graph classification problems on both synthetic and real-world datasets. We present three types of experiments: (i) synthetic graph experiment (see Figure 1), (ii) node classification on real-world graphs, and (iii) graph classification on point cloud models.

Node classification In this section, we empirically study the generalization gap in 8 real-world datasets. The task is to predict the label of a node given a set of features. The datasets vary in the number of nodes from 169, 343 to 3, 327, and in the number of edges from 1, 166, 243 to 9, 104. The feature dimension also varies from 8, 415 to 300 features, and the number of classes of the node label from 40 to 3. We consider the following datasets: *OGBN-Arxiv* (Wang et al., 2020; Mikolov et al., 2013), *Cora* (Yang et al., 2016b), *CiteSeer* (Yang et al., 2016b), *PubMed* (Yang et al., 2016b), *Coauthors CS* (Shchur et al., 2018), *Coauthors Physics* (Shchur et al., 2018), *Amazon-rating* (Platonov et al., 2023), and *Roman-Empire* (Platonov et al., 2023), details of the datasets can be found in Table 2. In all cases, we vary the number of nodes in the training set by partitioning it



(a) Differences of the outputs of GNNs with 2 layers.



(b) Differences of the outputs of GNNs with 3 layers.

Figure 8: Generalization gap as a function of number of nodes for average GNN output differences for graph classification over ModelNet10.

in $\{1, 2, 4, 8, 16, 32, 64, 32, 64, 128, 256, 512, 1024\}$ partitions when possible. For both the training and testing sets, we computed the loss in *cross-entropy loss*, and the accuracy in percentage (%).

Our main goal is to show that the rate presented in Theorem 1 holds in practice. That is to say, if we plot the logarithm of the generalization gap as a function of the logarithm of the number of nodes we see a linear rate. To be consistent with the theory, we also want to show that if the number of layers or the size of the features increases, so does the generalization gap.

In Figure 4, we plot the generalization gap of the accuracy in the logarithmic scale for a two-layered GNN (Figure 4a), and for a three-layered GNN (Figure 4b). On the upper side, we can see that the generalization bound decreases with the number of nodes and that outside of the strictly overfitting regime (when the training loss is below 95%), the generalization gap shows a linear decay, as depicted in the dashed line. The same behavior can be seen in Figures 4c, and 4d which correspond to the loss for 2 and 3 layered GNNs. As predicted by our theory, the generalization gap increases with the number of features and layers in the GNN. The behavior of the training and testing accuracy as a function of the number of nodes is intuitive. For the training loss, when the number of nodes in the training set is small, the GNN can overfit the training data. As the number of features increases, the GNN’s capacity to overfit also increases.

In Figures 5, and 6, we present the accuracy generalization gaps for 2 and 3 layers with 32 and 64 features. In the overfitting regime, the rate of our generalization bound seems to hold – decreases linearly with the number of nodes in the logarithmic scale. In the non-overfitting regime, our rate holds for the points whose training accuracy is below 95%. Also, we validate that the bound increases both with the number of features and the number of layers.

In Table 1, we present the Pearson correlation coefficient to measure the linear relationships in the generalization gaps of a 2 layers GNN with 64 hidden units in all datasets considered. In almost every case, the coefficient is above 0.95 which translates into a strong linear correlation. In Appendix we explain how we computed these values. As seen in the experiment, the GNN generalization gap experiences a linear decay with respect to the number of nodes in the logarithmic scale. Theorem 1 presents an upper bound on the generalization gap, whose rate can be seen to match the one seen in practice both for the loss, as well as the accuracy gaps.

Dataset	Pearson Correlation Coefficient
OGBN-Arxiv	-0.9980
Cora	-0.9686
CiteSeer	-0.9534
PubMed	-0.9761
CS	-0.8969
Physics	-0.9145
Amazon	-0.9972
Roman	-1.0000

Table 1: Pearson correlation for 2 layer, 64 hidden units GNNs measured on the accuracy generalization gap.

Spectral Continuity Constant Effect. To measure the impact of the spectral continuity constant C_L , we add a regularizer to the cross-entropy loss (see Appendix). We vary the value of the regularizer, noting that a larger regularizer translates into a smaller C_L and therefore a smoother function. In Figures 7a and 7c we see the empirical manifestation of the bound that we showed (cf. Theorem 1) – a GNN with a smaller C_L (a larger regularizer) will attain a smaller generalization gap. We can see that a larger regularizer (smaller continuity constant C_L , green line, regularizer 0.01) attains a smaller generalization gap, and as the regularization decreases

(C_L increases), the generalization gap increases. The effect of having smaller spectral continuity constants C_L is the lack of discriminability of the GNN. As can be seen in Figures 7b and 7d, the test error decreases when the multiplier is too large (C_L too small). Therefore, a spectral regularizer not too large can be shown to guarantee good test accuracy, but if the regularizer is too large, the test accuracy will be hurt by the lack of discriminability of the GNN as shown in Figure 7d. In all, we verify the fact that a GNN with a smoother spectral response will have a smaller generalization gap as shown in Theorem 1.

Graph classification We evaluate the generalization gap on graph prediction using the ModelNet10 dataset (Wu et al., 2015). We set the coordinates of each point as input graph signals, and the weights of the edges are calculated based on the Euclidean distance between the nodes. The generalization gap is calculated by training GNNs on graphs with $N = 20, 40 \dots, 100$ sampled points, and plotting the differences between the average output of the trained GNNs on the trained graph and a testing graph with size $N = 100$. Figure 8a shows the generalization gaps for GNNs with 2 layers and Figure 8b shows the results of GNNs with 3 layers. We can see that the output differences between the GNNs decrease with the number of nodes and decrease with the multiplier (increase with C_L). This verifies the claims of Theorem 2. In Appendix , we present experiment results on more model datasets.

Conclusion

We study the statistical generalization of GNNs from a manifold perspective. We consider graphs sampled from manifolds and prove that GNNs could effectively generalize to unseen data from the manifolds when the number of sampled points is large enough and the filter functions are continuous in the spectral domain. We verify our theoretical results on both synthetic and real-world datasets. The impact of this paper is to show a better understanding of GNN generalization capabilities from a spectral perspective relying on a continuous model. Our work also motivates the practical design of large-scale GNNs. Specifically, in order to achieve a better generalization, it is essential to restrict the discriminability of GNNs by putting assumptions on the spectral continuity of the filter functions in the GNNs. For future work, we will study the generalization of GNNs in more settings include transductive learning and out-of-distribution generalization. We are also willing to look into more application scenarios to fully utilize our theory on more complex and general manifold models. We will consider a better explanation and exploration deep into the overfitting regime of node classification, which is of great interest where the figures show that our proposed generalization upper bounds fit the rate.

References

- Eddie Aamari and Alexander Knop. Statistical query complexity of manifold estimation. In *Proceedings of the 53rd Annual ACM SIGACT Symposium on Theory of Computing*, pp. 116–122, 2021.
- Wolfgang Arendt, Robin Nittka, Wolfgang Peter, and Frank Steiner. Weyl’s law: Spectral properties of the laplacian in mathematics and physics. *Mathematical analysis of evolution, information, and complexity*, pp. 1–71, 2009.
- Mikhail Belkin and Partha Niyogi. Towards a theoretical foundation for laplacian-based manifold methods. *Journal of Computer and System Sciences*, 74(8):1289–1308, 2008.
- Monica Billio, Mila Getmansky, Andrew W Lo, and Lorian Pelizzon. Econometric measures of connectedness and systemic risk in the finance and insurance sectors. *Journal of financial economics*, 104(3):535–559, 2012.
- Michael M Bronstein, Joan Bruna, Yann LeCun, Arthur Szlam, and Pierre Vandergheynst. Geometric deep learning: going beyond euclidean data. *IEEE Signal Processing Magazine*, 34(4):18–42, 2017.
- Joan Bruna, Wojciech Zaremba, Arthur Szlam, and Yann LeCun. Spectral networks and locally connected networks on graphs. *arXiv preprint arXiv:1312.6203*, 2013.
- Jeff Calder and Nicolas Garcia Trillos. Improved spectral convergence rates for graph laplacians on ε -graphs and k-nn graphs. *Applied and Computational Harmonic Analysis*, 60:123–175, 2022.
- Juan Cervino, Luana Ruiz, and Alejandro Ribeiro. Learning by transference: Training graph neural networks on growing graphs. *IEEE Transactions on Signal Processing*, 71:233–247, 2023.
- Rudrasis Chakraborty, Jose Bouza, Jonathan H Manton, and Baba C Vemuri. Manifoldnet: A deep neural network for manifold-valued data with applications. *IEEE Transactions on Pattern Analysis and Machine Intelligence*, 44(2):799–810, 2020.
- Heeyoul Choi and Seungjin Choi. Kernel isomap. *Electronics letters*, 40(25):1612–1613, 2004.
- Weilin Cong, Morteza Ramezani, and Mehrdad Mahdavi. On provable benefits of depth in training graph convolutional networks. *Advances in Neural Information Processing Systems*, 34:9936–9949, 2021.
- Michaël Defferrard, Xavier Bresson, and Pierre Vandergheynst. Convolutional neural networks on graphs with fast localized spectral filtering. *Advances in neural information processing systems*, 29, 2016.
- Morris H. Degroot. Reaching a consensus. *Journal of the American Statistical Association*, 69(345):118–121, 1974. doi: 10.1080/01621459.1974.10480137. URL <https://www.tandfonline.com/doi/abs/10.1080/01621459.1974.10480137>.
- David B Dunson, Hau-Tieng Wu, and Nan Wu. Spectral convergence of graph laplacian and heat kernel reconstruction in l^∞ from random samples. *Applied and Computational Harmonic Analysis*, 55:282–336, 2021.
- Pascal Esser, Leena Chennuru Vankadara, and Debarghya Ghoshdastidar. Learning theory can (sometimes) explain generalisation in graph neural networks. *Advances in Neural Information Processing Systems*, 34: 27043–27056, 2021.
- Lawrence Craig Evans. *Measure theory and fine properties of functions*. Routledge, 2018.
- Wenqi Fan, Yao Ma, Qing Li, Jianping Wang, Guoyong Cai, Jiliang Tang, and Dawei Yin. A graph neural network framework for social recommendations. *IEEE Transactions on Knowledge and Data Engineering*, 34(5):2033–2047, 2020.
- Amir Massoud Farahmand, Csaba Szepesvári, and Jean-Yves Audibert. Manifold-adaptive dimension estimation. In *Proceedings of the 24th international conference on Machine learning*, pp. 265–272, 2007.
- Charles Fefferman, Sanjoy Mitter, and Hariharan Narayanan. Testing the manifold hypothesis. *Journal of the American Mathematical Society*, 29(4):983–1049, 2016.
- Meire Fortunato, Tobias Pfaff, Peter Wirnsberger, Alexander Pritzel, and Peter Battaglia. Multiscale mesh-graphnets. In *ICML 2022 2nd AI for Science Workshop*, 2022.

- Nicolás García Trillos, Moritz Gerlach, Matthias Hein, and Dejan Slepčev. Error estimates for spectral convergence of the graph laplacian on random geometric graphs toward the laplace–beltrami operator. *Foundations of Computational Mathematics*, 20(4):827–887, 2020.
- Vikas Garg, Stefanie Jegelka, and Tommi Jaakkola. Generalization and representational limits of graph neural networks. In *International Conference on Machine Learning*, pp. 3419–3430. PMLR, 2020.
- Justin Gilmer, Samuel S Schoenholz, Patrick F Riley, Oriol Vinyals, and George E Dahl. Neural message passing for quantum chemistry. In *International conference on machine learning*, pp. 1263–1272. PMLR, 2017.
- Alexander Grigor’yan. Heat kernels on weighted manifolds and applications. *Cont. Math*, 398(2006):93–191, 2006.
- Gal Gross and Eckhard Meinrenken. *Manifolds, vector fields, and differential forms: an introduction to differential geometry*. Springer Nature, 2023.
- Jiashu He, Charilaos I Kanatsoulis, and Alejandro Ribeiro. Network alignment with transferable graph autoencoders. *arXiv preprint arXiv:2310.03272*, 2023.
- Haotian Ju, Dongyue Li, Aneesh Sharma, and Hongyang R Zhang. Generalization in graph neural networks: Improved pac-bayesian bounds on graph diffusion. In *International Conference on Artificial Intelligence and Statistics*, pp. 6314–6341. PMLR, 2023.
- John Jumper, Richard Evans, Alexander Pritzel, Tim Green, Michael Figurnov, Olaf Ronneberger, Kathryn Tunyasuvunakool, Russ Bates, Augustin Žídek, Anna Potapenko, et al. Highly accurate protein structure prediction with alphafold. *Nature*, 596(7873):583–589, 2021.
- Kenji Kawaguchi, Leslie Pack Kaelbling, and Yoshua Bengio. Generalization in deep learning. *arXiv preprint arXiv:1710.05468*, 1(8), 2017.
- Nicolas Keriven, Alberto Bietti, and Samuel Vaiter. Convergence and stability of graph convolutional networks on large random graphs. *Advances in Neural Information Processing Systems*, 33:21512–21523, 2020.
- Thomas N Kipf and Max Welling. Semi-supervised classification with graph convolutional networks. In *International Conference on Learning Representations*, 2016.
- Remi Lam, Alvaro Sanchez-Gonzalez, Matthew Willson, Peter Wirnsberger, Meire Fortunato, Ferran Alet, Suman Ravuri, Timo Ewalds, Zach Eaton-Rosen, Weihua Hu, et al. Learning skillful medium-range global weather forecasting. *Science*, 382(6677):1416–1421, 2023.
- Thien Le and Stefanie Jegelka. Limits, approximation and size transferability for gnns on sparse graphs via graphops. *Advances in Neural Information Processing Systems*, 36, 2024.
- Jaekoo Lee, Hyunjae Kim, Jongsun Lee, and Sungroh Yoon. Transfer learning for deep learning on graph-structured data. In *Proceedings of the AAAI Conference on Artificial Intelligence*, volume 31, 2017.
- Ron Levie. A graphon-signal analysis of graph neural networks. *Advances in Neural Information Processing Systems*, 36, 2024.
- Ron Levie, Wei Huang, Lorenzo Bucci, Michael Bronstein, and Gitta Kutyniok. Transferability of spectral graph convolutional neural networks. *Journal of Machine Learning Research*, 22(272):1–59, 2021.
- Renjie Liao, Raquel Urtasun, and Richard Zemel. A pac-bayesian approach to generalization bounds for graph neural networks. In *International Conference on Learning Representations*, 2020.
- László Lovász. *Large networks and graph limits*, volume 60. American Mathematical Soc., 2012.
- Jiaqi Ma, Junwei Deng, and Qiaozhu Mei. Subgroup generalization and fairness of graph neural networks. *Advances in Neural Information Processing Systems*, 34:1048–1061, 2021.
- Sohir Maskey, Ron Levie, Yunseok Lee, and Gitta Kutyniok. Generalization analysis of message passing neural networks on large random graphs. *Advances in neural information processing systems*, 35:4805–4817, 2022.

- Sohir Maskey, Ron Levie, and Gitta Kutyniok. Transferability of graph neural networks: an extended graphon approach. *Applied and Computational Harmonic Analysis*, 63:48–83, 2023.
- Sohir Maskey, Gitta Kutyniok, and Ron Levie. Generalization bounds for message passing networks on mixture of graphons. *arXiv preprint arXiv:2404.03473*, 2024.
- Russell Merris. A survey of graph laplacians. *Linear and Multilinear Algebra*, 39(1-2):19–31, 1995.
- Tomas Mikolov, Ilya Sutskever, Kai Chen, Greg S Corrado, and Jeff Dean. Distributed representations of words and phrases and their compositionality. *Advances in neural information processing systems*, 26, 2013.
- Federico Monti, Davide Boscaini, Jonathan Masci, Emanuele Rodola, Jan Svoboda, and Michael M Bronstein. Geometric deep learning on graphs and manifolds using mixture model cnns. In *Proceedings of the IEEE conference on computer vision and pattern recognition*, pp. 5115–5124, 2017.
- Hariharan Narayanan and Partha Niyogi. On the sample complexity of learning smooth cuts on a manifold. In *COLT*, 2009.
- Alejandro Parada-Mayorga, Zhiyang Wang, and Alejandro Ribeiro. Graphon pooling for reducing dimensionality of signals and convolutional operators on graphs. *IEEE Transactions on Signal Processing*, 2023.
- Oleg Platonov, Denis Kuznedelev, Michael Diskin, Artem Babenko, and Liudmila Prokhorenkova. A critical look at the evaluation of gnns under heterophily: Are we really making progress? *arXiv preprint arXiv:2302.11640*, 2023.
- Raksha Ramakrishna, Hoi-To Wai, and Anna Scaglione. A user guide to low-pass graph signal processing and its applications: Tools and applications. *IEEE Signal Processing Magazine*, 37(6):74–85, 2020.
- Luana Ruiz, Luiz Chamon, and Alejandro Ribeiro. Graphon neural networks and the transferability of graph neural networks. *Advances in Neural Information Processing Systems*, 33:1702–1712, 2020.
- Luana Ruiz, Luiz FO Chamon, and Alejandro Ribeiro. Transferability properties of graph neural networks. *IEEE Transactions on Signal Processing*, 2023.
- Franco Scarselli, Marco Gori, Ah Chung Tsoi, Markus Hagenbuchner, and Gabriele Monfardini. The graph neural network model. *IEEE transactions on neural networks*, 20(1):61–80, 2008.
- Franco Scarselli, Ah Chung Tsoi, and Markus Hagenbuchner. The vapnik–chervonenkis dimension of graph and recursive neural networks. *Neural Networks*, 108:248–259, 2018.
- Oleksandr Shchur, Maximilian Mumme, Aleksandar Bojchevski, and Stephan Günnemann. Pitfalls of graph neural network evaluation. *arXiv preprint arXiv:1811.05868*, 2018.
- Weijing Shi and Raj Rajkumar. Point-gnn: Graph neural network for 3d object detection in a point cloud. In *Proceedings of the IEEE/CVF conference on computer vision and pattern recognition*, pp. 1711–1719, 2020.
- Yiqian Shi and Bin Xu. Gradient estimate of an eigenfunction on a compact riemannian manifold without boundary. *Annals of Global Analysis and Geometry*, 38:21–26, 2010.
- Alexey Strokach, David Becerra, Carles Corbi-Verge, Albert Perez-Riba, and Philip M Kim. Fast and flexible protein design using deep graph neural networks. *Cell systems*, 11(4):402–411, 2020.
- Ameet Talwalkar, Sanjiv Kumar, and Henry Rowley. Large-scale manifold learning. In *2008 IEEE Conference on Computer Vision and Pattern Recognition*, pp. 1–8. IEEE, 2008.
- Huayi Tang and Yong Liu. Towards understanding generalization of graph neural networks. In *International Conference on Machine Learning*, pp. 33674–33719. PMLR, 2023.
- Saurabh Verma and Zhi-Li Zhang. Stability and generalization of graph convolutional neural networks. In *Proceedings of the 25th ACM SIGKDD International Conference on Knowledge Discovery & Data Mining*, pp. 1539–1548, 2019.
- Ulrike Von Luxburg, Mikhail Belkin, and Olivier Bousquet. Consistency of spectral clustering. *The Annals of Statistics*, pp. 555–586, 2008.

- Kuansan Wang, Zhihong Shen, Chiyuan Huang, Chieh-Han Wu, Yuxiao Dong, and Anshul Kanakia. Microsoft academic graph: When experts are not enough. *Quantitative Science Studies*, 1(1):396–413, 2020.
- Zhiyang Wang, Mark Eisen, and Alejandro Ribeiro. Learning decentralized wireless resource allocations with graph neural networks. *IEEE Transactions on Signal Processing*, 70:1850–1863, 2022a.
- Zhiyang Wang, Luana Ruiz, and Alejandro Ribeiro. Convolutional neural networks on manifolds: From graphs and back. In *2022 56th Asilomar Conference on Signals, Systems, and Computers*, pp. 356–360. IEEE, 2022b.
- Zhiyang Wang, Luana Ruiz, and Alejandro Ribeiro. Geometric graph filters and neural networks: Limit properties and discriminability trade-offs. *IEEE Transactions on Signal Processing*, 2024a.
- Zhiyang Wang, Luana Ruiz, and Alejandro Ribeiro. Stability to deformations of manifold filters and manifold neural networks. *IEEE Transactions on Signal Processing*, pp. 1–15, 2024b. doi: 10.1109/TSP.2024.3378379.
- Yiming Wu and Kap Luk Chan. An extended isomap algorithm for learning multi-class manifold. In *Proceedings of 2004 International Conference on Machine Learning and Cybernetics (IEEE Cat. No. 04EX826)*, volume 6, pp. 3429–3433. IEEE, 2004.
- Zhirong Wu, Shuran Song, Aditya Khosla, Fisher Yu, Linguang Zhang, Xiaoou Tang, and Jianxiong Xiao. 3d shapenets: A deep representation for volumetric shapes. In *Proceedings of the IEEE conference on computer vision and pattern recognition*, pp. 1912–1920, 2015.
- Yuchen Xie, Jeffrey Ho, and Baba C Vemuri. Multiple atlas construction from a heterogeneous brain mr image collection. *IEEE transactions on medical imaging*, 32(3):628–635, 2013.
- Bo Yang, Ming Xiang, and Yupei Zhang. Multi-manifold discriminant isomap for visualization and classification. *Pattern Recognition*, 55:215–230, 2016a.
- Zhilin Yang, William Cohen, and Ruslan Salakhudinov. Revisiting semi-supervised learning with graph embeddings. In *International conference on machine learning*, pp. 40–48. PMLR, 2016b.
- Gilad Yehudai, Ethan Fetaya, Eli Meir, Gal Chechik, and Haggai Maron. From local structures to size generalization in graph neural networks. In *International Conference on Machine Learning*, pp. 11975–11986. PMLR, 2021.
- Xianchen Zhou and Hongxia Wang. The generalization error of graph convolutional networks may enlarge with more layers. *Neurocomputing*, 424:97–106, 2021.
- Qi Zhu, Carl Yang, Yidan Xu, Haonan Wang, Chao Zhang, and Jiawei Han. Transfer learning of graph neural networks with ego-graph information maximization. *Advances in Neural Information Processing Systems*, 34:1766–1779, 2021.

Contents

Introduction	1
Related works	2
Generalization bounds of GNNs	2
Neural networks on manifolds	3
Preliminaries	3
Graph neural networks	3
Manifold neural networks	4
Generalization analysis of GNNs based on manifolds	5
Manifold label prediction via node label prediction	5
Manifold classification via graph classification	7
Experiments	8
Conclusion	11
Induced manifold signals	17
Convergence of GNN to MNN	17
Local Lipschitz continuity of MNNs	21
Proof of Theorem 1	23
Proof of Theorem 2	25
Experiment details and further experiments	26
ModelNet10 and ModelNet40 graph classification tasks	26
Node classification training details and datasets	27
Spectral Continuity Constant Regularizer	27
Arxiv dataset	28
Cora dataset	28
CiteSeer dataset	28
PubMed dataset	28
Coauthors CS dataset	28
Coauthors Physics dataset	28
Heterophilous Amazon ratings dataset	28
Heterophilous Roman Empire dataset	31
Further references	32
Low Pass Filter Assumption	34

Induced manifold signals

The graph signal attached to this constructed graph \mathbf{G} can be seen as the discretization of the continuous function over the manifold. Suppose $f \in L^2(\mathcal{M})$, the graph signal \mathbf{x}_N is composed of discrete data values of the function f evaluated at X_N , i.e. $[\mathbf{x}_N]_i = f(x_i)$ for $i = 1, 2, \dots, N$. With a sampling operator $\mathbf{P}_N : L^2(\mathcal{M}) \rightarrow L^2(X_N)$, the discretization can be written as

$$\mathbf{x}_N = \mathbf{P}_N f. \quad (19)$$

Let μ_N be the empirical measure of the random sample as

$$\mu_N = \frac{1}{N} \sum_{i=1}^N \delta_{x_i}. \quad (20)$$

Let $\{V_i\}_{i=1}^N$ be the decomposition (García Trillos et al., 2020) of \mathcal{M} with respect to X_N with $V_i \subset B_r(x_i)$, where $B_r(x_i)$ denoted the closed metric ball of radius r centered at $x_i \in \mathcal{M}$. The decomposition can be achieved by the optimal transportation map $T : \mathcal{M} \rightarrow X_N$, which is defined by the ∞ -Optimal Transport distance between μ and μ_N .

$$d_\infty(\mu, \mu_N) := \min_{T: T_\# \mu = \mu_N} \text{esssup}_{x \in \mathcal{M}} d(x, T(x)), \quad (21)$$

where $T_\# \mu = \mu_N$ indicates that $\mu(T^{-1}(V)) = \mu_N(V)$ for every V_i of \mathcal{M} . This transportation map T induces the partition V_1, V_2, \dots, V_N of \mathcal{M} , where $V_i := T^{-1}(\{x_i\})$ with $\mu(V_i) = \frac{1}{N}$ for all $i = 1, \dots, N$. The radius of V_i can be bounded as $r \leq A(\log N/N)^{1/d}$ with A related to the geometry of \mathcal{M} (García Trillos et al., 2020, Theorem 2).

The manifold function induced by the graph signal \mathbf{x}_N over the sampled graph \mathbf{G} is defined by

$$(\mathbf{I}_N \mathbf{x}_N)(x) = \sum_{i=1}^N [\mathbf{x}]_i \mathbb{1}_{x \in V_i}, \text{ for all } x \in \mathcal{M} \quad (22)$$

where we denote $\mathbf{I}_N : L^2(X_N) \rightarrow L^2(\mathcal{M})$ as the inducing operator.

Convergence of GNN to MNN

The convergence of GNN on sampled graphs to MNN provides the support for the generalization analysis. We first introduce the inner product over the manifold. The inner product of signals $f, g \in L^2(\mathcal{M})$ is defined as

$$\langle f, g \rangle_{\mathcal{M}} = \int_{\mathcal{M}} f(x)g(x) d\mu(x), \quad (23)$$

where $d\mu(x)$ is the volume element with respect to the measure μ over \mathcal{M} . Similarly, the norm of the manifold signal f is

$$\|f\|_{\mathcal{M}}^2 = \langle f, f \rangle_{\mathcal{M}}. \quad (24)$$

Proposition 1. *Let $\mathcal{M} \subset \mathbb{R}^M$ be an embedded manifold with weighted Laplace operator \mathcal{L}_ρ and a bandlimited manifold signal f . Graph \mathbf{G}_N is constructed based on a set of N i.i.d. randomly sampled points $X_N = \{x_1, x_2, \dots, x_N\}$ according to measure μ over \mathcal{M} . A graph signal \mathbf{x} is the sampled manifold function values at X_N . The graph Laplacian \mathbf{L}_N is calculated based on (7) or (8) with ϵ as the graph parameter. Let $\Phi(\mathbf{H}, \mathcal{L}_\rho, \cdot)$ be a MNN on \mathcal{M} (6) with L layers and F features in each layer. Let $\Phi_{\mathbf{G}}(\mathbf{H}, \mathbf{L}_N, \cdot)$ be the GNN with the same architecture applied to the graph \mathbf{G}_N . Then, with the filters as low-pass and nonlinearities as normalized Lipschitz continuous, it holds in probability at least $1 - \delta$ that*

$$\frac{1}{N} \sum_{i=1}^N \|\Phi_{\mathbf{G}}(\mathbf{H}, \mathbf{L}_N, \mathbf{x}) - \mathbf{P}_N \Phi(\mathbf{H}, \mathcal{L}_\rho, \mathbf{I}_N \mathbf{x})\|_2 \leq LF^{L-1} \left(C_1 \epsilon + C_2 \sqrt{\frac{\log(1/\delta)}{N}} \right) \quad (25)$$

where C_1, C_2 are constants defined in the following proof.

Proposition 2. (Wang et al., 2024a, Proposition 2, Proposition 4) Let $\mathcal{M} \subset \mathbb{R}^M$ be equipped with Laplace operator \mathcal{L}_ρ , whose eigendecomposition is given by $\{\lambda_i, \phi_i\}_{i=1}^\infty$. Let \mathbf{L}_N be the discrete graph Laplacian of graph weights defined as (7) (or (8)), with spectrum $\{\lambda_{i,N}, \phi_{i,N}\}_{i=1}^N$. Fix $K \in \mathbb{N}^+$ and assume that $\epsilon = \epsilon(N) \geq (\log(C/\delta)/N)^{1/(d+4)}$ (or $\epsilon = \epsilon(N) \geq (\log(CN/\delta)/N)^{1/(d+4)}$). Then, with probability at least $1 - \delta$, we have

$$|\lambda_i - \lambda_{i,N}| \leq C_{\mathcal{M},1} \lambda_i \epsilon, \quad \|a_i \phi_{i,N} - \phi_i\| \leq C_{\mathcal{M},2} \frac{\lambda_i}{\theta_i} \epsilon, \quad (26)$$

with $a_i \in \{-1, 1\}$ for all $i < K$ and θ the eigengap of \mathcal{L} , i.e., $\theta_i = \min\{\lambda_i - \lambda_{i-1}, \lambda_{i+1} - \lambda_i\}$. The constants $C_{\mathcal{M},1}, C_{\mathcal{M},2}$ depend on d and the volume, the injectivity radius and sectional curvature of \mathcal{M} .

Proof. Because $\{x_1, x_2, \dots, x_N\}$ is a set of randomly sampled points from \mathcal{M} , based on Theorem 19 in Von Luxburg et al. (2008) we can claim that

$$|\langle \mathbf{P}_N f, \mathbf{P}_N \phi_i \rangle - \langle f, \phi_i \rangle_{\mathcal{M}}| = O\left(\sqrt{\frac{\log(1/\delta)}{N}}\right). \quad (27)$$

This also indicates that

$$\|\|\mathbf{P}_N f\|^2 - \|f\|_{\mathcal{M}}^2\| = O\left(\sqrt{\frac{\log(1/\delta)}{N}}\right), \quad (28)$$

which indicates $\|\mathbf{P}_N f\| = \|f\|_{\mathcal{M}} + O((\log(1/\delta)/N)^{1/4})$. We suppose that the input manifold signal is λ_M -bandlimited with M spectral components. We first write out the filter representation as

$$\|\mathbf{h}(\mathbf{L}_N) \mathbf{P}_N f - \mathbf{P}_N \mathbf{h}(\mathcal{L}_\rho) f\| = \left\| \sum_{i=1}^N \hat{h}(\lambda_{i,N}) \langle \mathbf{P}_N f, \phi_{i,N} \rangle \phi_{i,N} - \sum_{i=1}^M \hat{h}(\lambda_i) \langle f, \phi_i \rangle_{\mathcal{M}} \mathbf{P}_N \phi_i \right\| \quad (29)$$

$$\leq \left\| \sum_{i=1}^M \hat{h}(\lambda_{i,N}) \langle \mathbf{P}_N f, \phi_{i,N} \rangle \phi_{i,N} - \sum_{i=1}^M \hat{h}(\lambda_i) \langle f, \phi_i \rangle_{\mathcal{M}} \mathbf{P}_N \phi_i + \sum_{i=M+1}^N \hat{h}(\lambda_{i,N}) \langle \mathbf{P}_N f, \phi_{i,N} \rangle \phi_{i,N} \right\| \quad (30)$$

$$\leq \left\| \sum_{i=1}^M \hat{h}(\lambda_{i,N}) \langle \mathbf{P}_N f, \phi_{i,N} \rangle \phi_{i,N} - \sum_{i=1}^M \hat{h}(\lambda_i) \langle f, \phi_i \rangle_{\mathcal{M}} \mathbf{P}_N \phi_i \right\| + \left\| \sum_{i=M+1}^N \hat{h}(\lambda_{i,N}) \langle \mathbf{P}_N f, \phi_{i,N} \rangle \phi_{i,N} \right\| \quad (31)$$

The first part of (31) can be decomposed with the triangle inequality as

$$\begin{aligned} & \left\| \sum_{i=1}^M \hat{h}(\lambda_{i,N}) \langle \mathbf{P}_N f, \phi_{i,N} \rangle \phi_{i,N} - \sum_{i=1}^M \hat{h}(\lambda_i) \langle f, \phi_i \rangle_{\mathcal{M}} \mathbf{P}_N \phi_i \right\| \\ & \leq \left\| \sum_{i=1}^M (\hat{h}(\lambda_{i,N}) - \hat{h}(\lambda_i)) \langle \mathbf{P}_N f, \phi_{i,N} \rangle \phi_{i,N} \right\| + \left\| \sum_{i=1}^M \hat{h}(\lambda_i) (\langle \mathbf{P}_N f, \phi_{i,N} \rangle \phi_{i,N} - \langle f, \phi_i \rangle_{\mathcal{M}} \mathbf{P}_N \phi_i) \right\|. \end{aligned} \quad (32)$$

In equation (32), the first part relies on the difference of eigenvalues and the second part depends on the eigenvector difference. The first term in (32) is bounded with Cauchy-Schwartz inequality as

$$\left\| \sum_{i=1}^M (\hat{h}(\lambda_{i,N}) - \hat{h}(\lambda_i)) \langle \mathbf{P}_N f, \phi_{i,N} \rangle \phi_{i,N} \right\| \leq \sum_{i=1}^M |\hat{h}(\lambda_{i,N}) - \hat{h}(\lambda_i)| |\langle \mathbf{P}_N f, \phi_{i,N} \rangle| \quad (33)$$

$$\leq \|\mathbf{P}_N f\| \sum_{i=1}^M |\hat{h}'(\lambda_i)| |\lambda_{i,N} - \lambda_i| \quad (34)$$

$$\leq \|\mathbf{P}_N f\| \sum_{i=1}^M C_{\mathcal{M},1} C_L \epsilon \lambda_i^{-d} \quad (35)$$

$$\leq \|\mathbf{P}_N f\| C_L C_{\mathcal{M},1} \epsilon \sum_{i=1}^M i^{-2} \quad (36)$$

$$\leq \left(\|f\|_{\mathcal{M}} + \left(\frac{\log(1/\delta)}{N}\right)^{\frac{1}{4}} \right) C_{\mathcal{M},1} \epsilon \frac{\pi^2}{6} := A_1(N) \quad (37)$$

In (35), it depends on the low-pass filter assumption in Definition 4. In (36), we implement Weyl's law (Arendt et al., 2009) which indicates that eigenvalues of Laplace operator scales with the order $\lambda_i \sim i^{2/d}$. The last inequality comes from the fact that $\sum_{i=1}^{\infty} i^{-2} = \frac{\pi^2}{6}$. The second term in (32) can be bounded with the triangle inequality as

$$\begin{aligned} & \left\| \sum_{i=1}^M \hat{h}(\lambda_i) (\langle \mathbf{P}_N f, \phi_{i,N} \rangle \phi_{i,N} - \langle f, \phi_i \rangle_{\mathcal{M}} \mathbf{P}_N \phi_i) \right\| \\ & \leq \left\| \sum_{i=1}^M \hat{h}(\lambda_i) (\langle \mathbf{P}_N f, \phi_{i,N} \rangle \phi_{i,N} - \langle \mathbf{P}_N f, \phi_{i,N} \rangle \mathbf{P}_N \phi_i) \right\| \\ & \quad + \left\| \sum_{i=1}^M \hat{h}(\lambda_i) (\langle \mathbf{P}_N f, \phi_{i,N} \rangle \mathbf{P}_N \phi_i - \langle f, \phi_i \rangle_{\mathcal{M}} \mathbf{P}_N \phi_i) \right\| \end{aligned} \quad (38)$$

The first term in (38) can be bounded with inserting the eigenfunction convergence result in Proposition 2 as

$$\begin{aligned} & \left\| \sum_{i=1}^M \hat{h}(\lambda_i) (\langle \mathbf{P}_N f, \phi_{i,N} \rangle \phi_{i,N} - \langle \mathbf{P}_N f, \phi_{i,N} \rangle_{\mathcal{M}} \mathbf{P}_N \phi_i) \right\| \\ & \leq \sum_{i=1}^M \left| \hat{h}(\lambda_i) \right| \|\mathbf{P}_N f\| \|\phi_{i,N} - \mathbf{P}_N \phi_i\| \end{aligned} \quad (39)$$

$$\leq \sum_{i=1}^M (\lambda_i^{-d}) \frac{C_{\mathcal{M},2}\epsilon}{\theta_i} \left(\|f\|_{\mathcal{M}} + \left(\frac{\log(1/\delta)}{N} \right)^{\frac{1}{4}} \right) \quad (40)$$

$$\leq C_{\mathcal{M},2}\epsilon \frac{\pi^2}{6} \max_{i=1,\dots,M} \theta_i^{-1} \left(\|f\|_{\mathcal{M}} + \left(\frac{\log(1/\delta)}{N} \right)^{\frac{1}{4}} \right) \quad (41)$$

$$:= A_2(M, N). \quad (42)$$

Considering the low-pass filter assumption, the second term in (38) can be written as

$$\begin{aligned} & \left\| \sum_{i=1}^M \hat{h}(\lambda_{i,N}) (\langle \mathbf{P}_N f, \phi_{i,N} \rangle \mathbf{P}_N \phi_i - \langle f, \phi_i \rangle_{\mathcal{M}} \mathbf{P}_N \phi_i) \right\| \\ & \leq \sum_{i=1}^M \left| \hat{h}(\lambda_{i,N}) \right| |\langle \mathbf{P}_N f, \phi_{i,N} \rangle - \langle f, \phi_i \rangle_{\mathcal{M}}| \|\mathbf{P}_N \phi_i\| \end{aligned} \quad (43)$$

$$\leq \sum_{i=1}^M (\lambda_{i,N}^{-d}) |\langle \mathbf{P}_N f, \phi_{i,N} \rangle - \langle f, \phi_i \rangle_{\mathcal{M}}| \left(1 + \left(\frac{\log(1/\delta)}{N} \right)^{\frac{1}{4}} \right) \quad (44)$$

$$\leq \sum_{i=1}^M (1 + C_{\mathcal{M},1}\epsilon)^{-d} (\lambda_i^{-d}) |\langle \mathbf{P}_N f, \phi_{i,N} \rangle - \langle f, \phi_i \rangle_{\mathcal{M}}| \left(1 + \left(\frac{\log(1/\delta)}{N} \right)^{\frac{1}{4}} \right) \quad (45)$$

$$\leq \frac{\pi^2}{6} |\langle \mathbf{P}_N f, \phi_{i,N} \rangle - \langle f, \phi_i \rangle_{\mathcal{M}}| \left(1 + \left(\frac{\log(1/\delta)}{N} \right)^{\frac{1}{4}} \right) := A_3(N) \quad (46)$$

The term $|\langle \mathbf{P}_N f, \phi_{i,N} \rangle - \langle f, \phi_i \rangle_{\mathcal{M}}|$ can be decomposed by inserting a term $\langle \mathbf{P}_N f, \mathbf{P}_N \phi_i \rangle$ as

$$|\langle \mathbf{P}_N f, \phi_{i,N} \rangle - \langle f, \phi_i \rangle_{\mathcal{M}}| \leq |\langle \mathbf{P}_N f, \phi_{i,N} \rangle - \langle \mathbf{P}_N f, \mathbf{P}_N \phi_i \rangle + \langle \mathbf{P}_N f, \mathbf{P}_N \phi_i \rangle - \langle f, \phi_i \rangle_{\mathcal{M}}| \quad (47)$$

$$\leq |\langle \mathbf{P}_N f, \phi_{i,N} \rangle - \langle \mathbf{P}_N f, \mathbf{P}_N \phi_i \rangle| + |\langle \mathbf{P}_N f, \mathbf{P}_N \phi_i \rangle - \langle f, \phi_i \rangle_{\mathcal{M}}| \quad (48)$$

$$\leq \|\mathbf{P}_N f\| \|\phi_{i,N} - \mathbf{P}_N \phi_i\| + |\langle \mathbf{P}_N f, \mathbf{P}_N \phi_i \rangle - \langle f, \phi_i \rangle_{\mathcal{M}}| \quad (49)$$

$$\leq \left(\|f\|_{\mathcal{M}} + \left(\frac{\log(1/\delta)}{N} \right)^{\frac{1}{4}} \right) \frac{C_{\mathcal{M},2}\lambda_i\epsilon}{\theta_i} + \sqrt{\frac{\log(1/\delta)}{N}} \quad (50)$$

Then equation (45) can be bounded as

$$\begin{aligned} & \left\| \sum_{i=1}^M \hat{h}(\lambda_{i,N}) (\langle \mathbf{P}_N f, \phi_{i,N} \rangle \mathbf{P}_N \phi_i - \langle f, \phi_i \rangle_{\mathcal{M}} \mathbf{P}_N \phi_i) \right\| \\ & \leq \sum_{i=1}^M (1 + C_{\mathcal{M},1} \epsilon)^{-d} (\lambda_i^{-d}) \left(\left(\|f\|_{\mathcal{M}} + \left(\frac{\log(1/\delta)}{N} \right)^{\frac{1}{4}} \right) \frac{C_{\mathcal{M},2} \lambda_i \epsilon}{\theta_i} + \sqrt{\frac{\log(1/\delta)}{N}} \right) \left(1 + \left(\frac{\log(1/\delta)}{N} \right)^{\frac{1}{4}} \right) \end{aligned} \quad (51)$$

$$\leq \frac{\pi^2}{6} \max_{i=1, \dots, M} \frac{C_{\mathcal{M},2} \epsilon}{\theta_i} \left(\|f\|_{\mathcal{M}} + \left(\frac{\log(1/\delta)}{N} \right)^{\frac{1}{4}} \right) + \frac{\pi^2}{6} \sqrt{\frac{\log(1/\delta)}{N}} \quad (52)$$

The second term in (31) can be bounded with the eigenvalue difference bound in Proposition 2 as

$$\left\| \sum_{i=M+1}^N \hat{h}(\lambda_{i,N}) \langle \mathbf{P}_N f, \phi_{i,N} \rangle \phi_{i,N} \right\| \leq \sum_{i=M+1}^N (\lambda_{i,N}^{-d}) \left(\|f\|_{\mathcal{M}} + \left(\frac{\log(1/\delta)}{N} \right)^{\frac{1}{4}} \right) \quad (53)$$

$$\leq \sum_{i=M+1}^{\infty} (\lambda_{i,N}^{-d}) \|f\|_{\mathcal{M}} \quad (54)$$

$$\leq (1 + C_{\mathcal{M},1} \epsilon)^{-d} \sum_{i=M+1}^{\infty} (\lambda_i^{-d}) \|f\|_{\mathcal{M}} \quad (55)$$

$$\leq M^{-1} \|f\|_{\mathcal{M}} := A_4(M). \quad (56)$$

We note that the bound is made up by terms $A_1(N) + A_2(M, N) + A_3(N) + A_4(M)$, related to the bandwidth of manifold signal M and the number of sampled points N . This makes the bound scale with the order

$$\|\mathbf{h}(\mathbf{L}_N) \mathbf{P}_N f - \mathbf{P}_N \mathbf{h}(\mathcal{L}_\rho) f\| \leq C'_1 \epsilon + C'_2 \epsilon \theta_M^{-1} + C'_3 \sqrt{\frac{\log(1/\delta)}{N}} + C'_4 M^{-1}, \quad (57)$$

with $C'_1 = C_L C_{\mathcal{M},1} \frac{\pi^2}{6} \|f\|_{\mathcal{M}}$, $C'_2 = C_{\mathcal{M},2} \frac{\pi^2}{6}$, $C'_3 = \frac{\pi^2}{6}$ and $C'_4 = \|f\|_{\mathcal{M}}$. As N goes to infinity, for every $\delta > 0$, there exists some M_0 , such that for all $M > M_0$ it holds that $A_4(M) \leq \delta/2$. There also exists n_0 , such that for all $N > n_0$, it holds that $A_1(N) + A_2(M_0, N) + A_3(N) \leq \delta/2$. We can conclude that the summations converge as N goes to infinity. We see M large enough to have $M^{-1} \leq \delta'$, which makes the eigengap θ_M also bounded by some constant. We combine the first two terms as

$$\|\mathbf{h}(\mathbf{L}_N) \mathbf{P}_N f - \mathbf{P}_N \mathbf{h}(\mathcal{L}_\rho) f\| \leq (C_1 C_L + C_2) \epsilon + \frac{\pi^2}{6} \sqrt{\frac{\log(1/\delta)}{N}}, \quad (58)$$

with $C_1 = C_{\mathcal{M},1} \frac{\pi^2}{6} \|f\|_{\mathcal{M}}$ and $C_2 = C_{\mathcal{M},2} \frac{\pi^2}{6} \theta_{\delta'}^{-1}$. To bound the output difference of MNNs, we need to write in the form of features of the final layer

$$\|\Phi_{\mathbf{G}}(\mathbf{H}, \mathbf{L}_N, \mathbf{P}_N f) - \mathbf{P}_N \Phi(\mathbf{H}, \mathcal{L}_\rho, f)\| = \left\| \sum_{q=1}^F \mathbf{x}_{n,L}^q - \sum_{q=1}^F \mathbf{P}_N f_L^q \right\| \leq \sum_{q=1}^F \left\| \mathbf{x}_{n,L}^q - \mathbf{P}_N f_L^q \right\|. \quad (59)$$

By inserting the definitions, we have

$$\left\| \mathbf{x}_{n,l}^p - \mathbf{P}_N f_l^p \right\| = \left\| \sigma \left(\sum_{q=1}^F \mathbf{h}_l^{pq}(\mathbf{L}_N) \mathbf{x}_{n,l-1}^q \right) - \mathbf{P}_N \sigma \left(\sum_{q=1}^F \mathbf{h}_l^{pq}(\mathcal{L}_\rho) f_{l-1}^q \right) \right\| \quad (60)$$

with $\mathbf{x}_{n,0} = \mathbf{P}_N f$ as the input of the first layer. With a normalized point-wise Lipschitz nonlinearity, we have

$$\left\| \mathbf{x}_{n,l}^p - \mathbf{P}_N f_l^p \right\| \leq \left\| \sum_{q=1}^F \mathbf{h}_l^{pq}(\mathbf{L}_N) \mathbf{x}_{n,l-1}^q - \mathbf{P}_N \sum_{q=1}^F \mathbf{h}_l^{pq}(\mathcal{L}_\rho) f_{l-1}^q \right\| \quad (61)$$

$$\leq \sum_{q=1}^F \left\| \mathbf{h}_l^{pq}(\mathbf{L}_N) \mathbf{x}_{n,l-1}^q - \mathbf{P}_N \mathbf{h}_l^{pq}(\mathcal{L}_\rho) f_{l-1}^q \right\| \quad (62)$$

The difference can be further decomposed as

$$\begin{aligned} & \|\mathbf{h}_l^{pq}(\mathbf{L}_N)\mathbf{x}_{n,l-1}^q - \mathbf{P}_N\mathbf{h}_l^{pq}(\mathcal{L}_\rho)f_{l-1}^q\| \\ & \leq \|\mathbf{h}_l^{pq}(\mathbf{L}_N)\mathbf{x}_{n,l-1}^q - \mathbf{h}_l^{pq}(\mathbf{L}_N)\mathbf{P}_Nf_{l-1}^q + \mathbf{h}_l^{pq}(\mathbf{L}_N)\mathbf{P}_Nf_{l-1}^q - \mathbf{P}_N\mathbf{h}_l^{pq}(\mathcal{L}_\rho)f_{l-1}^q\| \end{aligned} \quad (63)$$

$$\leq \left\| \mathbf{h}_l^{pq}(\mathbf{L}_N)\mathbf{x}_{n,l-1}^q - \mathbf{h}_l^{pq}(\mathbf{L}_N)\mathbf{P}_Nf_{l-1}^q \right\| + \left\| \mathbf{h}_l^{pq}(\mathbf{L}_N)\mathbf{P}_Nf_{l-1}^q - \mathbf{P}_N\mathbf{h}_l^{pq}(\mathcal{L}_\rho)f_{l-1}^q \right\| \quad (64)$$

The second term can be bounded with (57) and we denote the bound as Δ_N for simplicity. The first term can be decomposed by Cauchy-Schwartz inequality and non-amplifying of the filter functions as

$$\left\| \mathbf{x}_{n,l}^p - \mathbf{P}_Nf_l^p \right\| \leq \sum_{q=1}^F \Delta_N \|\mathbf{x}_{n,l-1}^q\| + \sum_{q=1}^F \|\mathbf{x}_{l-1}^q - \mathbf{P}_Nf_{l-1}^q\|. \quad (65)$$

To solve this recursion, we need to compute the bound for $\|\mathbf{x}_l^p\|$. By normalized Lipschitz continuity of σ and the fact that $\sigma(0) = 0$, we can get

$$\|\mathbf{x}_l^p\| \leq \left\| \sum_{q=1}^F \mathbf{h}_l^{pq}(\mathbf{L}_N)\mathbf{x}_{l-1}^q \right\| \leq \sum_{q=1}^F \|\mathbf{h}_l^{pq}(\mathbf{L}_N)\| \|\mathbf{x}_{l-1}^q\| \leq \sum_{q=1}^F \|\mathbf{x}_{l-1}^q\| \leq F^{l-1}\|\mathbf{x}\|. \quad (66)$$

Insert this conclusion back to solve the recursion, we can get

$$\left\| \mathbf{x}_{n,l}^p - \mathbf{P}_Nf_l^p \right\| \leq lF^{l-1}\Delta_N\|\mathbf{x}\|. \quad (67)$$

Replace l with L we can obtain

$$\|\Phi_{\mathbf{G}}(\mathbf{H}, \mathbf{L}_N, \mathbf{P}_Nf) - \mathbf{P}_N\Phi(\mathbf{H}, \mathcal{L}_\rho, f)\| \leq LF^{L-1}\Delta_N, \quad (68)$$

when the input graph signal is normalized. By replacing $f = \mathbf{I}_N\mathbf{x}$, we can conclude the proof. \square

Local Lipschitz continuity of MNNs

We propose that the outputs of MNN defined in (6) are locally Lipschitz continuous within a certain area, which is stated explicitly as follows.

Proposition 3. (*Local Lipschitz continuity of MNNs*) Let MNN be L layers with F features in each layer, suppose the manifold filters are nonamplifying with $|\hat{h}(\lambda)| \leq 1$ and the nonlinearities normalized Lipschitz continuous, then there exists a constant C such that

$$|\Phi(\mathbf{H}, \mathcal{L}_\rho, f)(x) - \Phi(\mathbf{H}, \mathcal{L}_\rho, f)(y)| \leq F^L C' \text{dist}(x - y), \quad \text{for all } x, y \in B_r(\mathcal{M}), \quad (69)$$

where $B_r(\mathcal{M})$ is a ball with radius r over \mathcal{M} .

Proof. The output of MNN can be written explicitly as

$$|\Phi(\mathbf{H}, \mathcal{L}_\rho, f)(x) - \Phi(\mathbf{H}, \mathcal{L}_\rho, f)(y)| = \left| \sigma \left(\sum_{q=1}^F \mathbf{h}_L^q(\mathcal{L}_\rho)f_{L-1}^q(x) \right) - \sigma \left(\sum_{q=1}^F \mathbf{h}_L^q(\mathcal{L}_\rho)f_{L-1}^q(y) \right) \right| \quad (70)$$

$$\leq \left| \sum_{q=1}^F \mathbf{h}_L^q(\mathcal{L}_\rho)f_{L-1}^q(x) - \sum_{q=1}^F \mathbf{h}_L^q(\mathcal{L}_\rho)f_{L-1}^q(y) \right| \leq F \max_{q=1, \dots, F} |\mathbf{h}_L^q(\mathcal{L}_\rho)f_{L-1}^q(x) - \mathbf{h}_L^q(\mathcal{L}_\rho)f_{L-1}^q(y)|. \quad (71)$$

We have $f_{L-1}^q(x) = \sigma \left(\sum_{p=1}^F \mathbf{h}_{L-1}^p f_{L-2}^p(x) \right)$. The process can be repeated recursively, and finally, we can have

$$|\Phi(\mathbf{H}, \mathcal{L}_\rho, f)(x) - \Phi(\mathbf{H}, \mathcal{L}_\rho, f)(y)| \leq F^L |\mathbf{h}_L(\mathcal{L}_\rho) \cdots \mathbf{h}_1(\mathcal{L}_\rho)f(x) - \mathbf{h}_L(\mathcal{L}_\rho) \cdots \mathbf{h}_1(\mathcal{L}_\rho)f(y)|. \quad (72)$$

With f as a λ -bandlimited manifold signal, we suppose $g = \mathbf{h}_L(\mathcal{L}_\rho) \cdots \mathbf{h}_1(\mathcal{L}_\rho)f$. As $\langle f, \phi_i \rangle = 0$ for all $i > M$, g is also bandlimited and possesses M spectral components. The gradient can be bounded according to (Shi & Xu, 2010) combined with the non-amplifying property of the filter function as

$$\|\nabla g\|_\infty \leq C \sum_{\lambda_i \leq \lambda} \left| \hat{h}(\lambda_i) \right|^L \lambda_i^{\frac{d+1}{2}} \|f\|_{\mathcal{M}} \leq C \sum_{\lambda_i \leq \lambda} \lambda_i^{\frac{d+1}{2}} \|f\|_{\mathcal{M}} \quad (73)$$

From Theorem 4.5 in (Evans, 2018), g is locally Lipschitz continuous as

$$|g(x) - g(y)| \leq C' \text{dist}(x - y), \quad \text{with } x, y \in B_r(\mathcal{M}), \quad (74)$$

where $B_r(\mathcal{M})$ is a closed ball with radius r with C' depending on the geometry of \mathcal{M} .

Combining the above, we have the continuity of the output of MNN as

$$|\Phi(\mathbf{H}, \mathcal{L}_\rho, f)(x) - \Phi(\mathbf{H}, \mathcal{L}_\rho, f)(y)| \leq F^L C' \text{dist}(x - y), \quad \text{with } x, y \in B_r(\mathcal{M}), \quad (75)$$

which concludes the proof. \square

Proof of Theorem 1

Proof. To analyze the difference between the empirical risk and statistical risk, we introduce an intermediate term which is the induced version of the sampled MNN output. We define \mathbf{I}_N as the inducing operator based on the Voronoi decomposition $\{V_i\}_{i=1}^N$ defined in Section . This intermediate term is written explicitly as

$$\bar{\Phi}(\mathbf{H}, \mathcal{L}_\rho, f)(x) = \mathbf{I}_N \mathbf{P}_N \Phi(\mathbf{H}, \mathcal{L}_\rho, f)(x) = \sum_{i=1}^N \Phi(\mathbf{H}, \mathcal{L}_\rho, f)(x_i) \mathbb{1}_{x \in V_i}, \text{ for all } x \in \mathcal{M}, \quad (76)$$

where $x_i \in X_N$ are sampled points from the manifold.

Suppose $\mathbf{H} \in \arg \min_{\mathbf{H} \in \mathcal{H}} R_{\mathcal{M}}(\mathbf{H})$, we have

$$GA = \sup_{\mathbf{H} \in \mathcal{H}} |R_{\mathbf{G}}(\mathbf{H}) - R_{\mathcal{M}}(\mathbf{H})| \quad (77)$$

The difference between $R_{\mathbf{G}}(\mathbf{H})$ and $R_{\mathcal{M}}(\mathbf{H})$ can be decomposed as

$$\begin{aligned} & |R_{\mathbf{G}}(\mathbf{H}) - R_{\mathcal{M}}(\mathbf{H})| \\ &= \left| \frac{1}{N} \sum_{i=1}^N \ell([\Phi_{\mathbf{G}}(\mathbf{H}, \mathbf{L}_N, \mathbf{x})]_i, [\mathbf{y}]_i) - \int_{\mathcal{M}} \ell(\Phi(\mathbf{H}, \mathcal{L}_\rho, f)(x), g(x)) \, \mathrm{d}\mu(x) \right| \end{aligned} \quad (78)$$

$$\begin{aligned} &= \left| \frac{1}{N} \sum_{i=1}^N \ell([\Phi_{\mathbf{G}}(\mathbf{H}, \mathbf{L}_N, \mathbf{x})]_i, [\mathbf{y}]_i) - \int_{\mathcal{M}} \ell(\bar{\Phi}(\mathbf{H}, \mathcal{L}_\rho, f)(x), g(x)) \, \mathrm{d}\mu(x) \right. \\ &\quad \left. + \int_{\mathcal{M}} \ell(\bar{\Phi}(\mathbf{H}, \mathcal{L}_\rho, f)(x), g(x)) \, \mathrm{d}\mu(x) - \int_{\mathcal{M}} \ell(\Phi(\mathbf{H}, \mathcal{L}_\rho, f)(x), g(x)) \, \mathrm{d}\mu(x) \right| \end{aligned} \quad (79)$$

$$\begin{aligned} &\leq \left| \frac{1}{N} \sum_{i=1}^N \ell([\Phi_{\mathbf{G}}(\mathbf{H}, \mathbf{L}_N, \mathbf{x})]_i, [\mathbf{y}]_i) - \int_{\mathcal{M}} \ell(\bar{\Phi}(\mathbf{H}, \mathcal{L}_\rho, f)(x), g(x)) \, \mathrm{d}\mu(x) \right| \\ &\quad + \left| \int_{\mathcal{M}} \ell(\bar{\Phi}(\mathbf{H}, \mathcal{L}_\rho, f)(x), g(x)) \, \mathrm{d}\mu(x) - \int_{\mathcal{M}} \ell(\Phi(\mathbf{H}, \mathcal{L}_\rho, f)(x), g(x)) \, \mathrm{d}\mu(x) \right| \end{aligned} \quad (80)$$

We analyze the two terms in (80) separately, with the first term bounded based on the convergence of GNN to MNN and the second term bounded with the smoothness of manifold functions.

The first term in (80) can be written as

$$\left| \frac{1}{N} \sum_{i=1}^N \ell([\Phi_{\mathbf{G}}(\mathbf{H}, \mathbf{L}_N, \mathbf{x})]_i, [\mathbf{y}]_i) - \int_{\mathcal{M}} \ell(\bar{\Phi}(\mathbf{H}, \mathcal{L}_\rho, f)(x), g(x)) \, \mathrm{d}\mu(x) \right| \quad (81)$$

$$= \frac{1}{N} \left| \sum_{i=1}^N \ell([\Phi_{\mathbf{G}}(\mathbf{H}, \mathbf{L}_N, \mathbf{x})]_i, [\mathbf{y}]_i) - \sum_{i=1}^N \ell(\Phi(\mathbf{H}, \mathcal{L}_\rho, f)(x_i), g(x_i)) \right| \quad (82)$$

$$\leq \frac{1}{N} \sum_{i=1}^N |\ell([\Phi_{\mathbf{G}}(\mathbf{H}, \mathbf{L}_N, \mathbf{x})]_i, [\mathbf{y}]_i) - \ell(\Phi(\mathbf{H}, \mathcal{L}_\rho, f)(x_i), g(x_i))| \quad (83)$$

$$\leq \frac{1}{N} \sum_{i=1}^N \left| [\Phi_{\mathbf{G}}(\mathbf{H}, \mathbf{L}_N, \mathbf{x})]_i - \Phi(\mathbf{H}, \mathcal{L}_\rho, f)(x_i) \right| \quad (84)$$

$$\leq \frac{1}{N} \|\Phi_{\mathbf{G}}(\mathbf{H}, \mathbf{L}_N, \mathbf{x}) - \mathbf{P}_N \Phi(\mathbf{H}, \mathcal{L}_\rho, \mathbf{I}_N \mathbf{x})\|_1 \quad (85)$$

$$\leq \frac{1}{\sqrt{N}} L F^{L-1} \left((C_1 C_L + C_2) \epsilon + \frac{\pi^2}{6} \sqrt{\frac{\log(1/\delta)}{N}} \right) \quad (86)$$

From (81) to (82), we use the definition of induced manifold signal defined in (76). We utilize the Lipschitz continuity assumption on loss function from (83) to (84). From (84) to (85), it depends on the fact that \mathbf{x} is a single-entry vector and that $[\mathbf{y}]_i$ is the value sampled from target manifold function g evaluated on x_i . Finally the bound depends on the convergence of GNN on the sampled graph to the MNN as stated in Proposition 1.

The second term is decomposed as

$$\left| \int_{\mathcal{M}} \ell(\bar{\Phi}(\mathbf{H}, \mathcal{L}_\rho, f)(x), g(x)) \, \mathbf{d}\mu(x) - \int_{\mathcal{M}} \ell(\Phi(\mathbf{H}, \mathcal{L}_\rho, f)(x), g(x)) \, \mathbf{d}\mu(x) \right| \quad (87)$$

$$\leq \left| \sum_{i=1}^N \int_{V_i} \ell(\bar{\Phi}(\mathbf{H}, \mathcal{L}_\rho, f)(x), g(x)) \, \mathbf{d}\mu(x) - \sum_{i=1}^N \int_{V_i} \ell(\Phi(\mathbf{H}, \mathcal{L}_\rho, f)(x), g(x)) \, \mathbf{d}\mu(x) \right| \quad (88)$$

$$\leq \sum_{i=1}^N \int_{V_i} |\ell(\bar{\Phi}(\mathbf{H}, \mathcal{L}_\rho, f)(x), g(x)) - \ell(\Phi(\mathbf{H}, \mathcal{L}_\rho, f)(x), g(x))| \, \mathbf{d}\mu(x) \quad (89)$$

$$\leq \sum_{i=1}^N \int_{V_i} |\bar{\Phi}(\mathbf{H}, \mathcal{L}_\rho, f)(x) - \Phi(\mathbf{H}, \mathcal{L}_\rho, f)(x)| \, \mathbf{d}\mu(x) \quad (90)$$

$$\leq \sum_{i=1}^N \int_{V_i} |\Phi(\mathbf{H}, \mathcal{L}_\rho, f)(x_i) - \Phi(\mathbf{H}, \mathcal{L}_\rho, f)(x)| \, \mathbf{d}\mu(x) \quad (91)$$

From (87) to (88), it relies on the decomposition of the MNN output over $\{V_i\}_{i=1}^N$. From (89) to (90), we use the Lipschitz continuity of loss function. From (90) to (91), we use the definition of $\bar{\Phi}(\mathbf{H}, \mathcal{L}_\rho, f)$. Proposition 3 indicates that the MNN outputs are Lipschitz continuous within a certain range, which leads to

$$\begin{aligned} & \sum_{i=1}^N \int_{V_i} |\Phi(\mathbf{H}, \mathcal{L}_\rho, f)(x_i) - \Phi(\mathbf{H}, \mathcal{L}_\rho, f)(x)| \, \mathbf{d}\mu(x) \\ & \leq \sum_{i=1}^N \int_{V_i} F^L C_3 \left(\frac{\log N}{N} \right)^{\frac{1}{d}} \, \mathbf{d}\mu(x) \end{aligned} \quad (92)$$

$$= F^L C_3 \left(\frac{\log N}{N} \right)^{\frac{1}{d}} \sum_{i=1}^N \int_{V_i} \mathbf{d}\mu(x) \quad (93)$$

$$\leq F^L C_3 \left(\frac{\log N}{N} \right)^{\frac{1}{d}}. \quad (94)$$

Combining (86) and (92), we can conclude the proof. \square

Proof of Theorem 2

Proof. We can write the difference as

$$\begin{aligned} & |R_{\mathbf{G}}(\mathbf{H}) - R_{\mathcal{M}}(\mathbf{H})| \\ & \leq \sum_{k=1}^K \left| \ell \left(\frac{1}{N} \sum_{i=1}^N [\Phi_{\mathbf{G}}(\mathbf{H}, \mathbf{L}_{N,k}, \mathbf{x}_k)]_i, y_k \right) - \ell \left(\int_{\mathcal{M}_k} \Phi(\mathbf{H}, \mathcal{L}_{\rho,k}, f_k) d\mu_k(x), y_k \right) \right| \end{aligned} \quad (95)$$

Based on the property of absolute value inequality and the Lipschitz continuity assumption of loss function (Assumption 2), we have

$$\begin{aligned} & \left| \ell \left(\frac{1}{N} \sum_{i=1}^N [\Phi_{\mathbf{G}}(\mathbf{H}, \mathbf{L}_{N,k}, \mathbf{x}_k)]_i, y_k \right) - \ell \left(\int_{\mathcal{M}_k} \Phi(\mathbf{H}, \mathcal{L}_{\rho,k}, f_k) d\mu_k(x), y_k \right) \right| \\ & \leq \left| \frac{1}{N} \sum_{i=1}^N [\Phi_{\mathbf{G}}(\mathbf{H}, \mathbf{L}_{N,k}, \mathbf{x}_k)]_i - \int_{\mathcal{M}_k} \Phi(\mathbf{H}, \mathcal{L}_{\rho,k}, f_k) d\mu_k(x) \right| \end{aligned} \quad (96)$$

We insert an intermediate term $\Phi(\mathbf{H}, \mathcal{L}_{\rho,k}, f_k)(x_i)$ as the value evaluated on the sampled point x_i , which leads to

$$\left| \frac{1}{N} \sum_{i=1}^N [\Phi_{\mathbf{G}}(\mathbf{H}, \mathbf{L}_{N,k}, \mathbf{x}_k)]_i - \int_{\mathcal{M}_k} \Phi(\mathbf{H}, \mathcal{L}_{\rho,k}, f_k) d\mu_k(x) \right| \quad (97)$$

$$\begin{aligned} & \leq \left| \frac{1}{N} \sum_{i=1}^N [\Phi_{\mathbf{G}}(\mathbf{H}, \mathbf{L}_{N,k}, \mathbf{x}_k)]_i - \frac{1}{N} \sum_{i=1}^N \Phi(\mathbf{H}, \mathcal{L}_{\rho,k}, f_k)(x_i) \right| + \\ & \quad \left| \frac{1}{N} \sum_{i=1}^N \Phi(\mathbf{H}, \mathcal{L}_{\rho,k}, f_k)(x_i) - \int_{\mathcal{M}_k} \Phi(\mathbf{H}, \mathcal{L}_{\rho,k}, f_k) d\mu_k(x) \right| \end{aligned} \quad (98)$$

The first term in (98) can be bounded similarly as (85), which is explicitly written as

$$\left| \frac{1}{N} \sum_{i=1}^N [\Phi_{\mathbf{G}}(\mathbf{H}, \mathbf{L}_{N,k}, \mathbf{x}_k)]_i - \frac{1}{N} \sum_{i=1}^N \Phi(\mathbf{H}, \mathcal{L}_{\rho,k}, f_k)(x_i) \right| \quad (99)$$

$$\leq \frac{1}{N} \|\Phi_{\mathbf{G}}(\mathbf{H}, \mathbf{L}_N, \mathbf{x}_k) - \mathbf{P}_N \Phi(\mathbf{H}, \mathcal{L}_{\rho,k}, f_k)\|_1 \quad (100)$$

$$\leq \frac{1}{\sqrt{N}} \|\Phi_{\mathbf{G}}(\mathbf{H}, \mathbf{L}_N, \mathbf{x}_k) - \mathbf{P}_N \Phi(\mathbf{H}, \mathcal{L}_{\rho,k}, f_k)\|_2 \quad (101)$$

$$\leq \frac{1}{\sqrt{N}} \left((C_1 C_L + C_2) \epsilon + \frac{\pi^2}{6} \sqrt{\frac{\log(1/\delta)}{N}} \right) \quad (102)$$

The second term is

$$\left| \frac{1}{N} \sum_{i=1}^N \Phi(\mathbf{H}, \mathcal{L}_{\rho,k}, f_k)(x_i) - \int_{\mathcal{M}_k} \Phi(\mathbf{H}, \mathcal{L}_{\rho,k}, f_k) d\mu_k(x) \right| \quad (103)$$

$$= \left| \sum_{i=1}^N \int_{V_i} \Phi(\mathbf{H}, \mathcal{L}_{\rho,k}, f_k)(x_i) d\mu_k(x) - \sum_{i=1}^N \int_{V_i} \Phi(\mathbf{H}, \mathcal{L}_{\rho,k}, f_k)(x) d\mu_k(x) \right| \quad (104)$$

$$\leq \sum_{i=1}^N \int_{V_i} |\Phi(\mathbf{H}, \mathcal{L}_{\rho,k}, f_k)(x_i) - \Phi(\mathbf{H}, \mathcal{L}_{\rho,k}, f_k)(x)| d\mu_k(x) \quad (105)$$

$$\leq F^L C_3 \left(\frac{\log N}{N} \right)^{\frac{1}{d}} \quad (106)$$

This depends on the Lipschitz continuity of the output manifold function in Proposition 3. \square

Experiment details and further experiments

All experiments were done using a *NVIDIA GeForce RTX 3090*, and each set of experiments took at most 10 hours to complete. In total, we run 10 datasets, which amounts for around 100 hours of GPU use. All datasets used in this paper are public, and free to use. They can be downloaded using the *pytorch* package (<https://pytorch-geometric.readthedocs.io/en/latest/modules/datasets.html>), the *ogb* package (<https://ogb.stanford.edu/docs/nodeprop/>) and the Princeton ModelNet project (<https://modelnet.cs.princeton.edu/>). In total, the datasets occupy around 5 gb. However, they do not need to be all stored at the same time, as the experiments that we run can be done in series.

ModelNet10 and ModelNet40 graph classification tasks

ModelNet10 dataset (Wu et al., 2015) includes 3,991 meshed CAD models from 10 categories for training and 908 models for testing as Figure 9 shows. ModelNet40 dataset includes 38,400 training and 9,600 testing models as Figure 10 shows. In each model, N points are uniformly randomly selected to construct graphs to approximate the underlying model, such as chairs, tables.

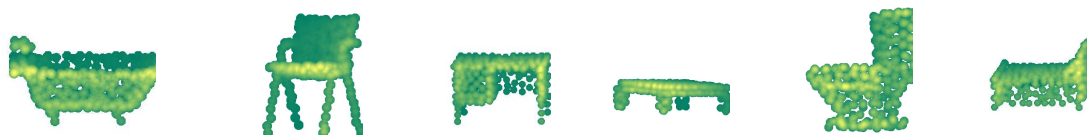


Figure 9: Point cloud models in ModelNet10 with $N = 300$ sampled points in each model, corresponding to bathtub, chair, desk, table, toiler, and bed.

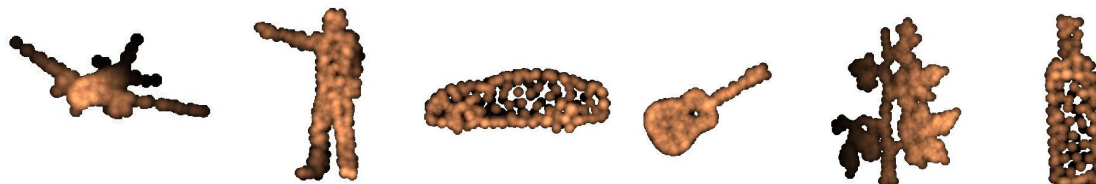


Figure 10: Point cloud models from ModelNet40 with $N = 300$ sampled points in each model, corresponding to airplane, person, car, guitar, plant, and bottle.

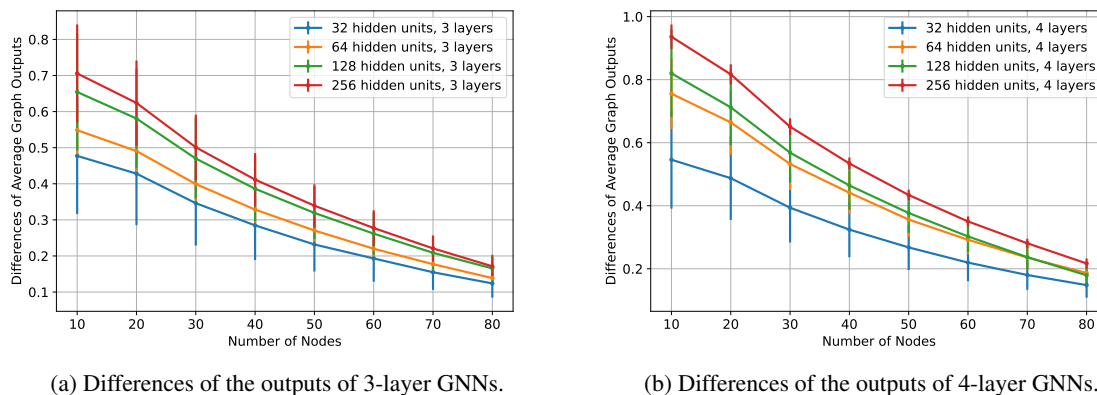


Figure 11: Graph outputs differences of GNNs with different architectures on ModelNet40 dataset.

The weight function of the constructed graph is determined as (7) with $\epsilon = 0.1$. We calculate the Laplacian matrix for each graph as the input graph shift operator. In this experiment, we implement GNNs with different numbers of layers and hidden units with $K = 5$ filters in each layer. All the GNN architectures are trained by minimizing the cross-entropy loss. We implement an ADAM optimizer with the learning rate set as 0.005 along with the forgetting factors 0.9 and 0.999. We carry out the training for 40 epochs with the size of batches set as 10. We run 5 random dataset partitions and show the average performances and the standard deviation across these partitions.

Node classification training details and datasets

In this section, we present the results for node classification. In this paragraph we present the common details for all datasets, we will next delve into each specific detail inside the dataset subsection that follows.

Name	Nodes	Edges	Features	Number of Classes	Reference
Arxiv	169,343	1,166,243	128	40	Wang et al. (2020); Mikolov et al. (2013)
Cora	2,708	10,556	1,433	7	Yang et al. (2016b)
CiteSeer	3,327	9,104	3,703	6	Yang et al. (2016b)
PubMed	19,717	88,648	500	3	Yang et al. (2016b)
Coauthor Physics	18,333	163,788	6,805	15	Shchur et al. (2018)
Coauthor CS	34,493	495,924	8,415	5	Shchur et al. (2018)
Amazon-ratings	24,492	93,050	300	5	Platonov et al. (2023)
Roman-empire	22,662	32,927	300	18	Platonov et al. (2023)

Table 2: Details of the datasets considered in the experiments.

In all datasets, we used the graph convolutional layer GCN, and trained for 1000 epochs. For the optimizer, we used AdamW, with using a learning rate of 0.01, and 0 weight decay. We trained using the graph convolutional layer, with a varying number of layers and hidden units. For dropout, we used 0.5. We trained using the cross-entropy loss. In all cases, we trained 2 and 3 layered GNNs.

To compute the linear approximation in the plots, we used the mean squared error estimator of the form

$$\mathbf{y} = s * \log(\mathbf{n}) + p. \tag{107}$$

Where s is the slope, p is the point, and \mathbf{n} is the vector with the nodes in the training set for each experiment. Note that we repeated each experiment for 10 independent runs. In all experiments, we compute the value of s and p that minimize the mean square error over the mean of the experiment runs, and we compute the Pearson correlation index over those values.

Our experiment shows that our bound shows the same rate dependency as the experiments. That is to say, in the logarithmic scale, the generalization gap of GNNs is linear with respect to the logarithm of the number of nodes. In most cases, the Pearson correlation index is above 0.9 in absolute value, which indicates a strong linear relationship. We noticed that the linear relationship changes the slope in the overfitting regime, and in the non-overfitting regime. That is to say, when the GNN is overfitting the training set, the generalization gap decreases at a much slower rate than it does with the GNN does not have the capacity to do so. Therefore, in the case in which the GNN overfits the training set for all nodes when computed s using all the samples in the experiment. On the other hand, when the number of nodes is large enough that the GNN cannot overfit the training set, then we computed the s and p with the nodes in the non overfitting regime.

Spectral Continuity Constant Regularizer

We add a regularization term to the loss to better control the value of the spectral continuity constant (defined in Definition 4) while training. To do so, given a convolutional filter $\mathbf{h} \in \mathbb{R}^K$, its associated spectral continuity constant is

$$R(\mathbf{h}) = \sum_{k=0}^{K-1} k|h_k|\lambda_{max}^{k-1}, \tag{108}$$

Where λ_{max} is the largest eigenvalue of the graph \mathbf{G} .

Arxiv dataset

For this datasets, we trained 2, 3, 4 layered GNN. We also used a learning rate scheduler `ReduceLROnPlateau` with mode min, factor 0.5, patience 100 and a minimum learning rate of 0.001.

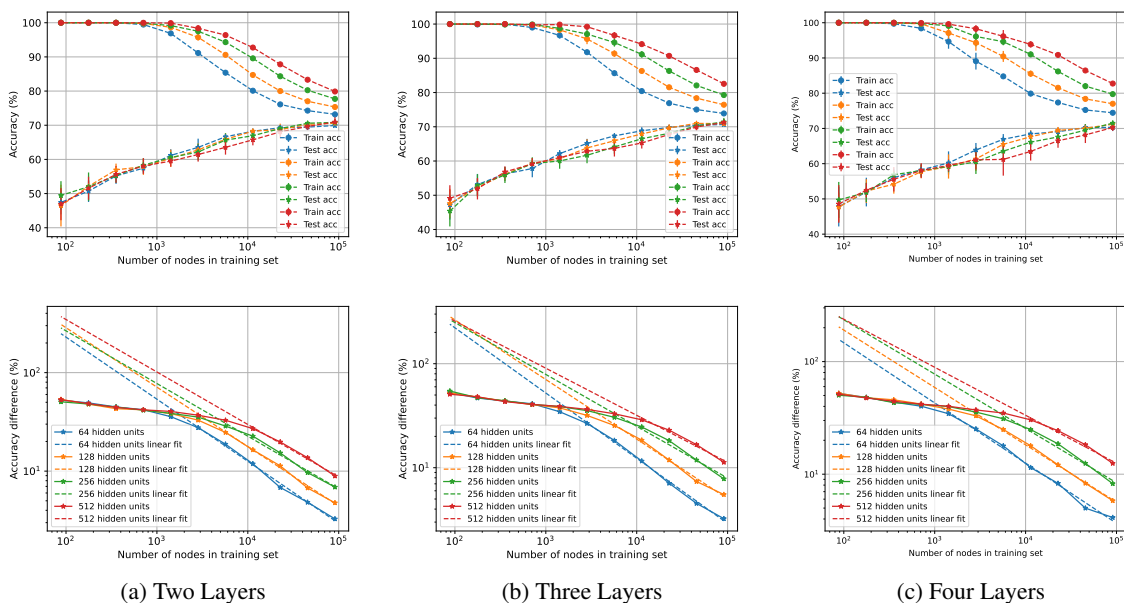


Figure 12: Generalization gap for the OGBN-Arxiv dataset on the accuracy as a function of the number of nodes in the training set.

Cora dataset

For the Cora dataset, we used the standard one, which can be obtained running `torch_geometric.datasets.Planetoid(ro`

CiteSeer dataset

For the CiteSeer dataset, we used the standard one, which can be obtained running `torch_geometric.datasets.Planetoid(ro`

PubMed dataset

For the PubMed dataset, we used the standard one, which can be obtained running `torch_geometric.datasets.Planetoid(ro`

Coauthors CS dataset

For the CS dataset, we used the standard one, which can be obtained running `torch_geometric.datasets.Coauthor(ro`. In this case, given that there are no training and testing sets, we randomly partitioned the datasets and used 90% of the samples for training and the remaining 10% for testing.

Coauthors Physics dataset

For the Physics dataset, we used the standard one, which can be obtained running `torch_geometric.datasets.Coauthor(ro`. In this case, given that there are no training and testing sets, we randomly partitioned the datasets and used 90% of the samples for training and the remaining 10% for testing.

Heterophilous Amazon ratings dataset

For the Amazon dataset, we used the standard one, which can be obtained running `torch_geometric.datasets.Heterophil`. In this case, we used the 10 different splits that the dataset has assigned.

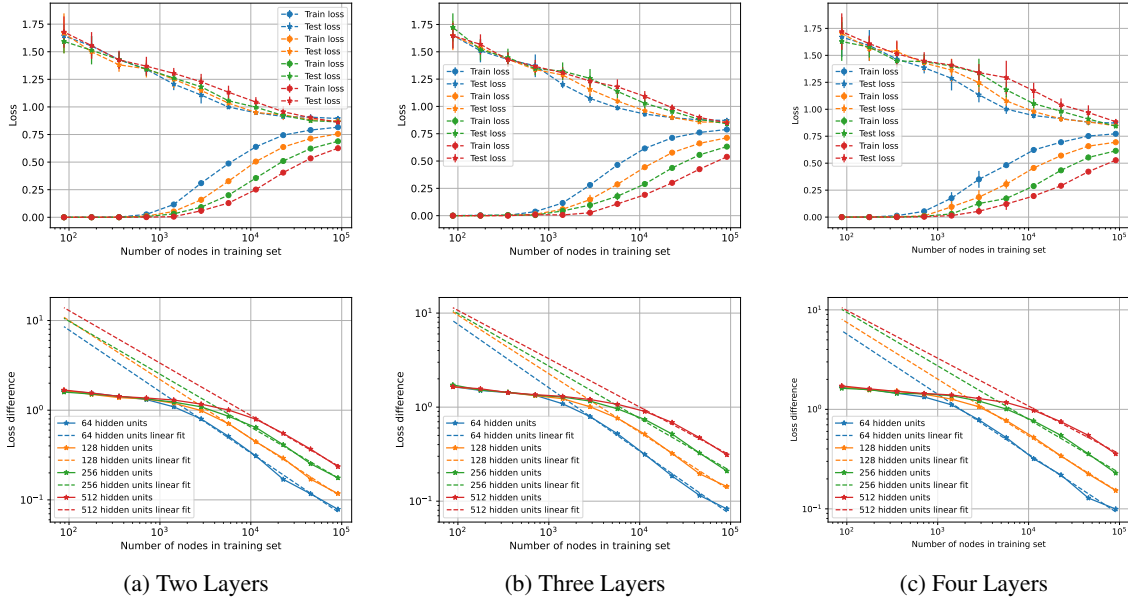


Figure 13: Generalization gap for the OGBN-arxiv dataset on the loss (cross-entropy) as a function of the number of nodes in the training set.

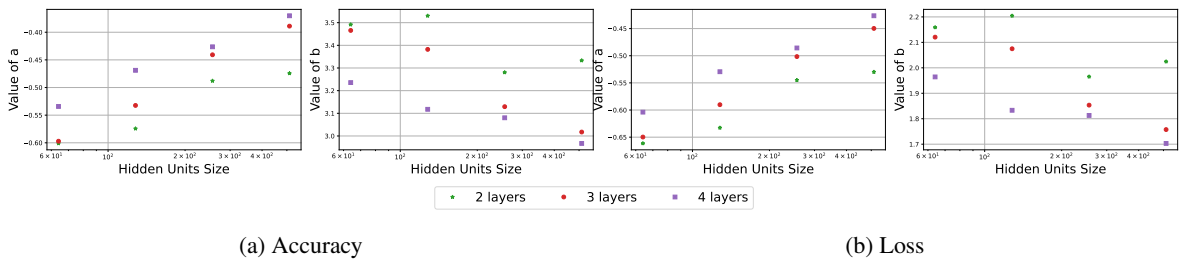


Figure 14: Values of slope (a) and point (b) corresponding to the linear fit ($a * \log(N) + b$) of Figures 13 and 12.

Type	Lay.	Feat.	Slope	Point	Pearson Correlation Coefficient
Accuracy	2	64	$-6.301e-01$	$3.621e+00$	$-9.980e-01$
Accuracy	2	128	$-6.034e-01$	$3.663e+00$	$-9.985e-01$
Accuracy	2	256	$-5.347e-01$	$3.493e+00$	$-9.952e-01$
Accuracy	2	512	$-5.328e-01$	$3.605e+00$	$-9.975e-01$
Accuracy	3	64	$-6.271e-01$	$3.600e+00$	$-9.987e-01$
Accuracy	3	128	$-5.730e-01$	$3.567e+00$	$-9.970e-01$
Accuracy	3	256	$-4.986e-01$	$3.393e+00$	$-9.910e-01$
Accuracy	3	512	$-4.529e-01$	$3.315e+00$	$-9.934e-01$
Accuracy	4	64	$-5.343e-01$	$3.236e+00$	$-9.971e-01$
Accuracy	4	128	$-5.096e-01$	$3.299e+00$	$-9.987e-01$
Accuracy	4	256	$-4.827e-01$	$3.337e+00$	$-9.920e-01$
Accuracy	4	512	$-4.264e-01$	$3.229e+00$	$-9.927e-01$
Loss	2	64	$-6.853e-01$	$2.265e+00$	$-9.975e-01$
Loss	2	128	$-6.562e-01$	$2.311e+00$	$-9.988e-01$
Loss	2	256	$-5.907e-01$	$2.174e+00$	$-9.968e-01$
Loss	2	512	$-5.848e-01$	$2.280e+00$	$-9.989e-01$
Loss	3	64	$-6.739e-01$	$2.228e+00$	$-9.980e-01$
Loss	3	128	$-6.229e-01$	$2.224e+00$	$-9.976e-01$
Loss	3	256	$-5.581e-01$	$2.111e+00$	$-9.942e-01$
Loss	3	512	$-5.141e-01$	$2.057e+00$	$-9.955e-01$
Loss	4	64	$-6.039e-01$	$1.964e+00$	$-9.980e-01$
Loss	4	128	$-5.701e-01$	$2.014e+00$	$-9.991e-01$
Loss	4	256	$-5.379e-01$	$2.051e+00$	$-9.951e-01$
Loss	4	512	$-4.810e-01$	$1.957e+00$	$-9.937e-01$

Table 3: Details of the linear approximation of the Arxiv Dataset. Note that in this case, we used only the values of the generalization gap whose training error is below 95%.

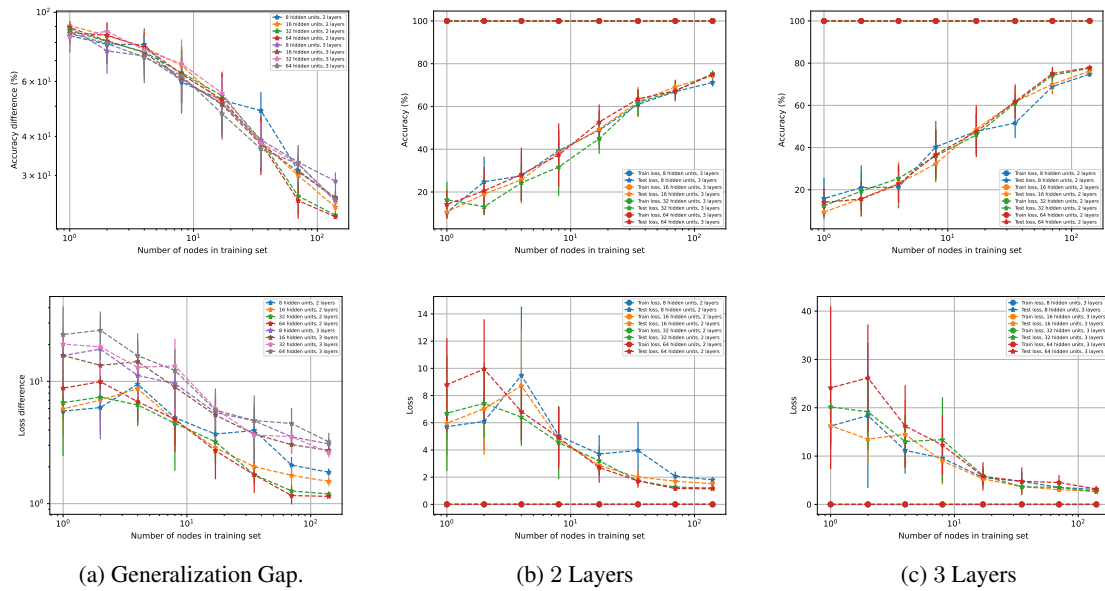


Figure 15: Generalization gap, testing, and training losses with respect to the number of nodes in the Cora dataset. The top row is in accuracy, and the bottom row is the cross-entropy loss.

Type	Lay.	Feat.	Slope	Point	Pearson Correlation Coefficient
Accuracy	2	16	$-2.839e - 01$	$2.022e + 00$	$-9.803e - 01$
Accuracy	2	32	$-2.917e - 01$	$2.014e + 00$	$-9.690e - 01$
Accuracy	2	64	$-3.006e - 01$	$2.021e + 00$	$-9.686e - 01$
Accuracy	3	16	$-2.656e - 01$	$1.996e + 00$	$-9.891e - 01$
Accuracy	3	32	$-2.637e - 01$	$2.008e + 00$	$-9.679e - 01$
Accuracy	3	64	$-2.581e - 01$	$1.981e + 00$	$-9.870e - 01$
Loss	2	16	$-3.631e - 01$	$9.406e - 01$	$-9.250e - 01$
Loss	2	32	$-4.228e - 01$	$9.638e - 01$	$-9.657e - 01$
Loss	2	64	$-4.991e - 01$	$1.067e + 00$	$-9.776e - 01$
Loss	3	16	$-4.131e - 01$	$1.276e + 00$	$-9.753e - 01$
Loss	3	32	$-4.605e - 01$	$1.385e + 00$	$-9.730e - 01$
Loss	3	64	$-4.589e - 01$	$1.455e + 00$	$-9.756e - 01$

Table 4: Details of the linear approximation of the Cora Dataset. Note that in this case we used all the values given that the training accuracy is 100% for all nodes.

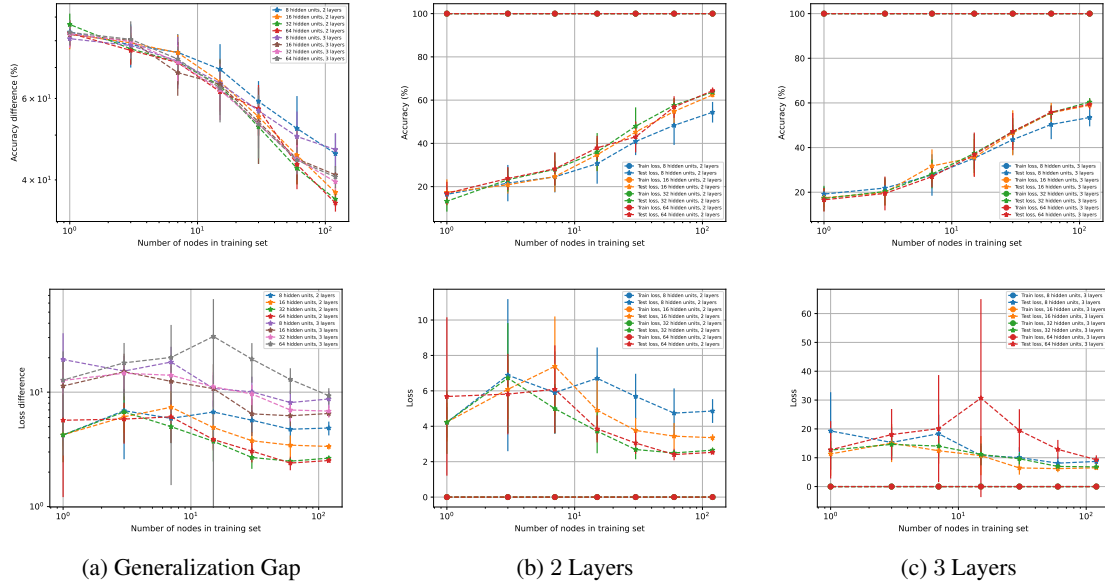


Figure 16: Generalization gap, testing, and training losses with respect to the number of nodes in the CiteSeer dataset. The top row is in accuracy, and the bottom row is the cross-entropy loss.

Heterophilous Roman Empire dataset

For the Roman dataset, we used the standard one, which can be obtained running `torch_geometric.datasets.HeterophilousRomanEmpire`. In this case, we used the 10 different splits that the dataset has assigned.

Type	Lay.	Feat.	Slope	Point	Pearson Correlation Coefficient
Accuracy	2	16	$-1.699e - 01$	$1.972e + 00$	$-9.518e - 01$
Accuracy	2	32	$-1.856e - 01$	$1.978e + 00$	$-9.714e - 01$
Accuracy	2	64	$-1.749e - 01$	$1.966e + 00$	$-9.534e - 01$
Accuracy	3	16	$-1.585e - 01$	$1.956e + 00$	$-9.721e - 01$
Accuracy	3	32	$-1.659e - 01$	$1.963e + 00$	$-9.721e - 01$
Accuracy	3	64	$-1.658e - 01$	$1.967e + 00$	$-9.702e - 01$
Loss	2	16	$-1.049e - 01$	$7.757e - 01$	$-5.924e - 01$
Loss	2	32	$-1.762e - 01$	$7.646e - 01$	$-7.981e - 01$
Loss	2	64	$-2.186e - 01$	$8.384e - 01$	$-9.120e - 01$
Loss	3	16	$-1.802e - 01$	$1.169e + 00$	$-8.345e - 01$
Loss	3	32	$-1.629e - 01$	$1.200e + 00$	$-8.767e - 01$
Loss	3	64	$-5.917e - 02$	$1.283e + 00$	$-2.562e - 01$

Table 5: Details of the linear approximation of the CiteSeer Dataset. Note that in this case we used all the values given that the training accuracy is 100% for all nodes.

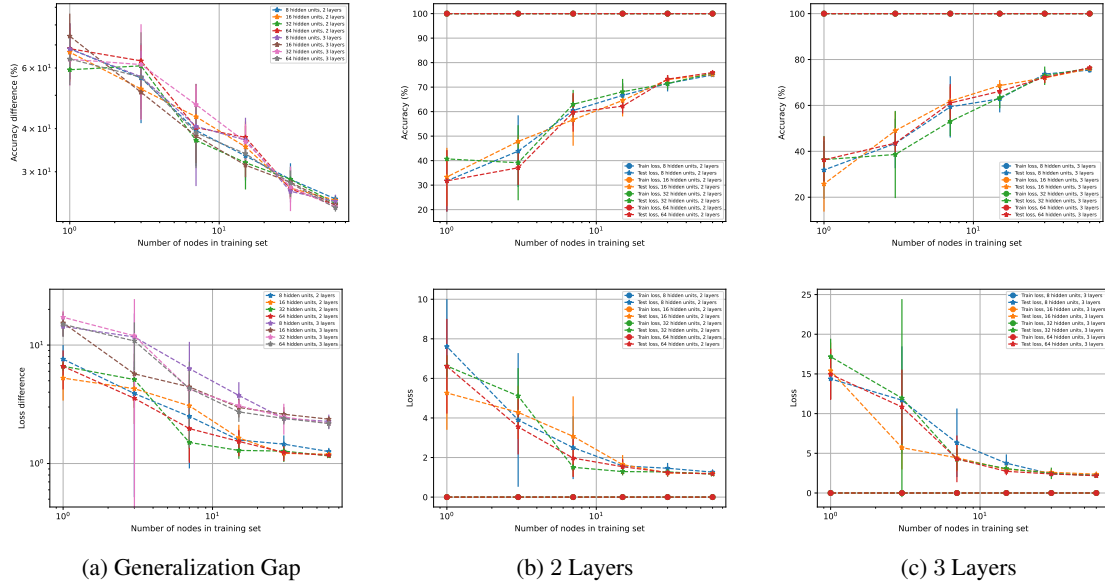


Figure 17: Generalization gap, testing, and training losses with respect to the number of nodes in the PubMed dataset. The top row is in accuracy, and the bottom row is the cross-entropy loss.

Further references

Graphon theory Different from the manifold model we’re using, some research constructs graphs derived from graphons, which can be viewed as a random limit graph model. This research has focused on their convergence, stability, as well as transferability (Ruiz et al., 2020; Maskey et al., 2023; Keriven et al., 2020). In (Parada-Mayorga et al., 2023), graphon is used as a pooling tool in GNNs. Despite its utility, the graphon presents several limitations compared to the manifold model we use. Firstly, the graphon model assumes an infinite degree at every node (Lovász, 2012), which is not the case in the manifold model. Additionally, graphons offer limited insight into the underlying model; visualizing a graphon is challenging, except in the stochastic block model case. Manifolds, however, are more interpretable, especially when based on familiar shapes like spheres and 3D models (see Figure 2). Finally, the manifold model supports a wider range of characterizable models, making it a more realistic choice.

Type	Lay.	Feat.	Slope	Point	Pearson Correlation Coefficient
Accuracy	2	16	$-2.523e - 01$	$1.834e + 00$	$-9.942e - 01$
Accuracy	2	32	$-2.433e - 01$	$1.812e + 00$	$-9.583e - 01$
Accuracy	2	64	$-2.764e - 01$	$1.869e + 00$	$-9.761e - 01$
Accuracy	3	16	$-2.748e - 01$	$1.844e + 00$	$-9.910e - 01$
Accuracy	3	32	$-2.661e - 01$	$1.861e + 00$	$-9.712e - 01$
Accuracy	3	64	$-2.558e - 01$	$1.827e + 00$	$-9.890e - 01$
Loss	2	16	$-4.166e - 01$	$7.695e - 01$	$-9.718e - 01$
Loss	2	32	$-4.733e - 01$	$7.852e - 01$	$-9.137e - 01$
Loss	2	64	$-4.368e - 01$	$7.547e - 01$	$-9.718e - 01$
Loss	3	16	$-4.424e - 01$	$1.067e + 00$	$-9.549e - 01$
Loss	3	32	$-5.518e - 01$	$1.223e + 00$	$-9.655e - 01$
Loss	3	64	$-5.246e - 01$	$1.169e + 00$	$-9.632e - 01$

Table 6: Details of the linear approximation of the PubMed Dataset. Note that in this case we used all the values given that the training accuracy is 100% for all nodes.

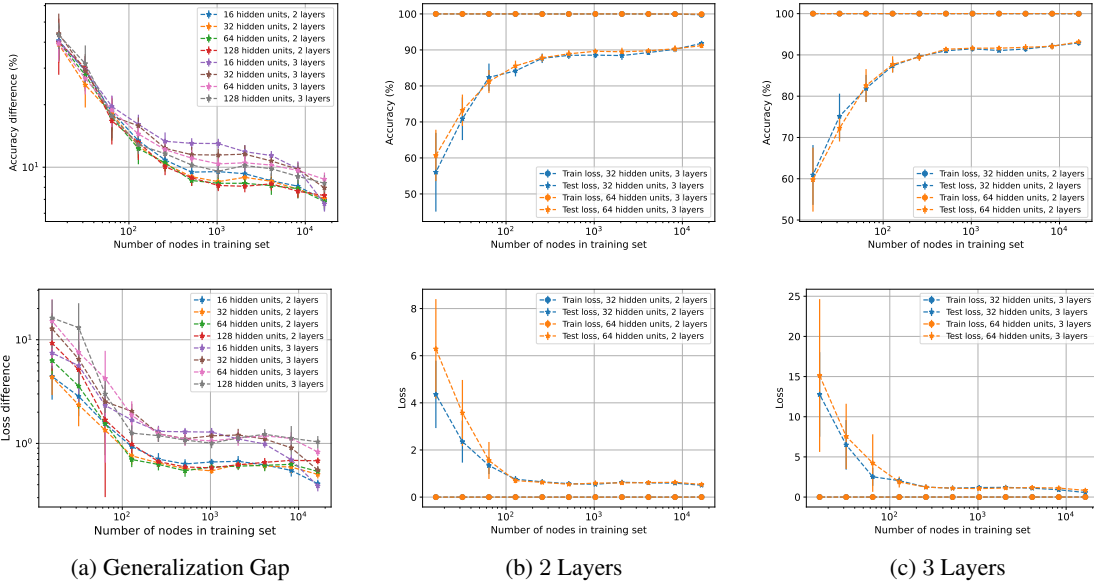


Figure 18: Generalization gap, testing, and training losses with respect to the number of nodes in the CS dataset. The top row is in accuracy, and the bottom row is the cross-entropy loss.

Transferability of GNNs The transferability of GNNs has been extensively studied by examining the differences in GNN outputs across graphs of varying sizes as they converge to a limit model. This analysis, however, often lacks statistical generalization. Several studies have explored GNN transferability with graphon models, proving bounds on the differences in GNN outputs (Ruiz et al., 2023, 2020; Maskey et al., 2023). Other research has demonstrated how increasing graph size during GNN training can improve generalization to large-scale graphs (Cervino et al., 2023). The transferability of GNNs has also been investigated in the context of graphs generated from general topological spaces (Levie et al., 2021) and manifolds (Wang et al., 2024a). Furthermore, a novel graphop operator has been proposed as a limit model for both dense and sparse graphs, with proven transferability results (Le & Jegelka, 2024). Further research has focused on transfer learning for GNNs by measuring distances between graphs without assuming a limit model (Lee et al., 2017; Zhu et al., 2021). Finally, a transferable graph transformer has been proposed and empirically validated (He et al., 2023).

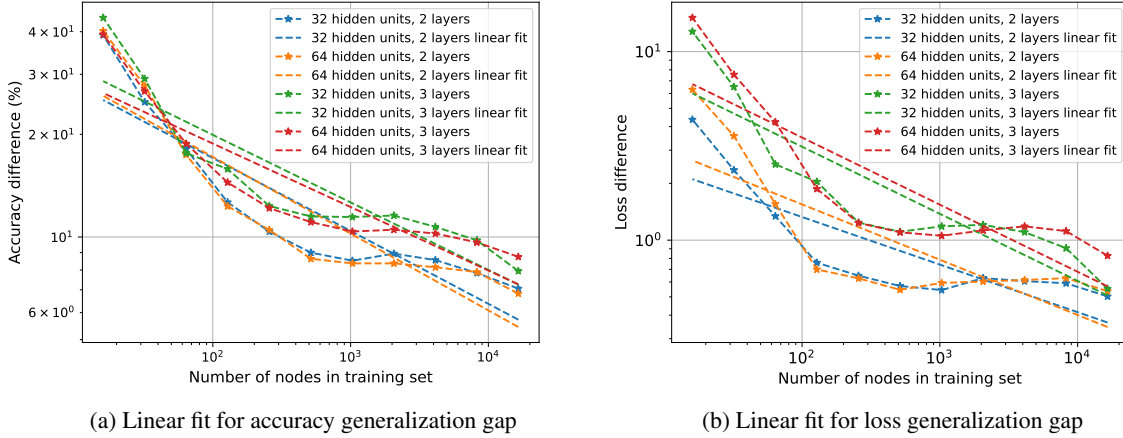


Figure 19: Generalization gaps as a function of the number of nodes in the training set in the CS dataset.

Type	Lay.	Feat.	Slope	Point	Pearson Correlation Coefficient
Accuracy	2	32	$-2.138e-01$	$1.659e+00$	$-9.007e-01$
Accuracy	2	64	$-2.250e-01$	$1.685e+00$	$-8.969e-01$
Accuracy	3	32	$-1.979e-01$	$1.695e+00$	$-9.009e-01$
Accuracy	3	64	$-1.862e-01$	$1.646e+00$	$-8.980e-01$
Loss	2	32	$-2.523e-01$	$6.273e-01$	$-8.244e-01$
Loss	2	64	$-2.933e-01$	$7.762e-01$	$-7.925e-01$
Loss	3	32	$-3.558e-01$	$1.207e+00$	$-8.924e-01$
Loss	3	64	$-3.560e-01$	$1.256e+00$	$-8.568e-01$

Table 7: Details of the linear approximation of the CS Dataset. Note that in this case we used all the values given that the training accuracy is 100% for all nodes.

Type	Lay.	Feat.	Slope	Point	Pearson Correlation Coefficient
Accuracy	2	32	$-1.524e-01$	$1.235e+00$	$-9.064e-01$
Accuracy	2	64	$-1.478e-01$	$1.218e+00$	$-9.145e-01$
Accuracy	3	32	$-1.227e-01$	$1.190e+00$	$-9.328e-01$
Accuracy	3	64	$-1.268e-01$	$1.200e+00$	$-8.826e-01$
Loss	2	32	$-1.111e-01$	$-5.257e-02$	$-7.591e-01$
Loss	2	64	$-9.684e-02$	$-7.335e-02$	$-7.696e-01$
Loss	3	32	$-1.410e-01$	$2.875e-01$	$-8.280e-01$
Loss	3	64	$-1.068e-01$	$2.388e-01$	$-7.679e-01$

Table 8: Details of the linear approximation of the Physics Dataset. Note that in this case we used all the values given that the training accuracy is 100% for all nodes.

Low Pass Filter Assumption

In the main results, we assume that the GNN and MNN are low-pass filters. This is a reasonable assumption because high-frequency signals on graphs or manifolds can fluctuate significantly between adjacent entries, leading to instability and learning challenges. We expect a degree of local homogeneity, which translates to low-frequency signals. This assumption is supported by empirical evidence in various domains, including opinion dynamics, econometrics, and graph signal processing (Degroot, 1974; Billio et al., 2012; Ramakrishna

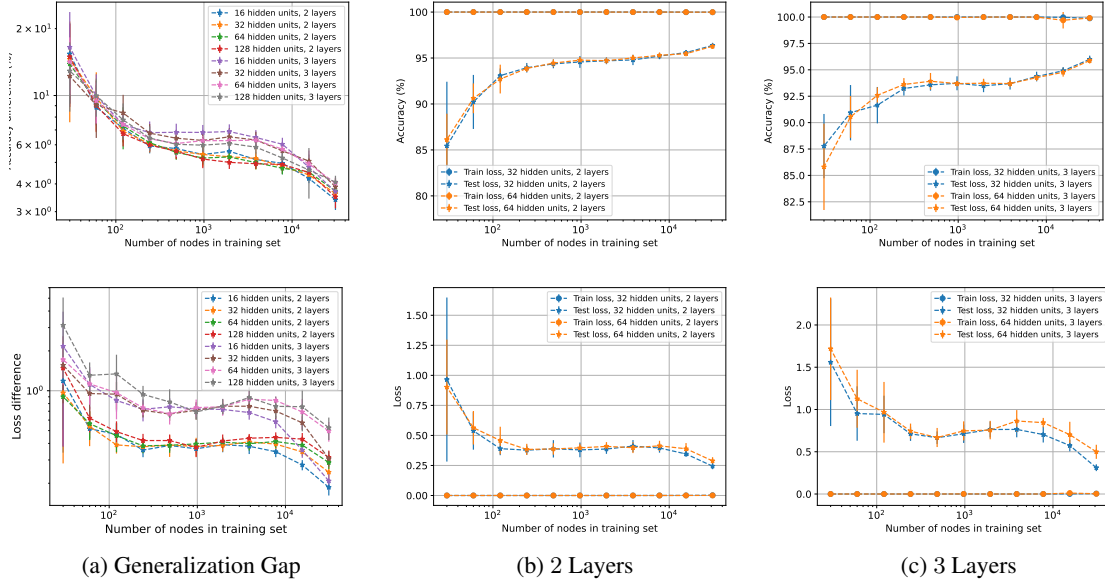


Figure 20: Generalization gap, testing, and training losses with respect to the number of nodes in the Physics dataset. The top row is in accuracy, and the bottom row is the cross-entropy loss.

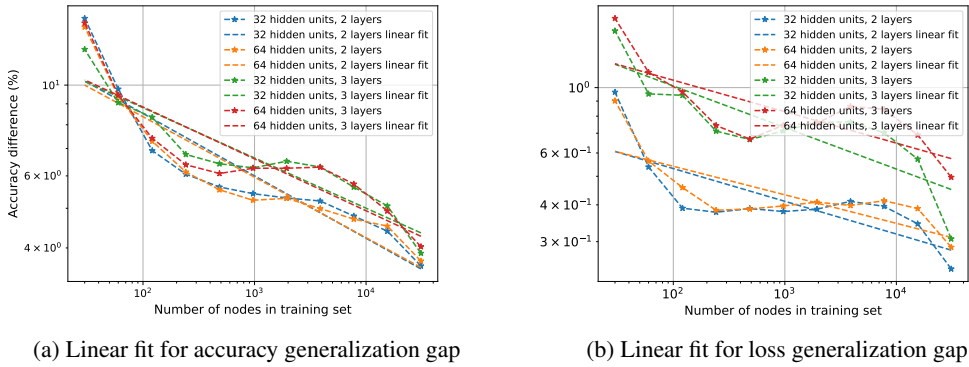


Figure 21: Generalization Gaps as a function of the number of nodes in the training set in the Physics dataset.

Type	Lay.	Feat.	Slope	Point	Pearson Correlation Coefficient
Accuracy	2	32	$-7.693e-01$	$4.236e+00$	$-9.914e-01$
Accuracy	2	64	$-7.788e-01$	$4.404e+00$	$-9.972e-01$
Accuracy	3	32	$-7.268e-01$	$4.101e+00$	$-9.868e-01$
Accuracy	3	64	$-7.354e-01$	$4.257e+00$	$-9.921e-01$
Loss	2	32	$-1.086e+00$	$3.971e+00$	$-9.968e-01$
Loss	2	64	$-1.096e+00$	$4.189e+00$	$-9.985e-01$
Loss	3	32	$-1.134e+00$	$4.339e+00$	$-9.965e-01$
Loss	3	64	$-1.154e+00$	$4.629e+00$	$-9.991e-01$

Table 9: Details of the linear approximation of the Amazon Dataset. Note that in this case we used only the values of the generalization gap whose training error is below 95%.

et al., 2020).

Moreover, several other effective learning techniques, such as Principal Component Analysis (PCA) and

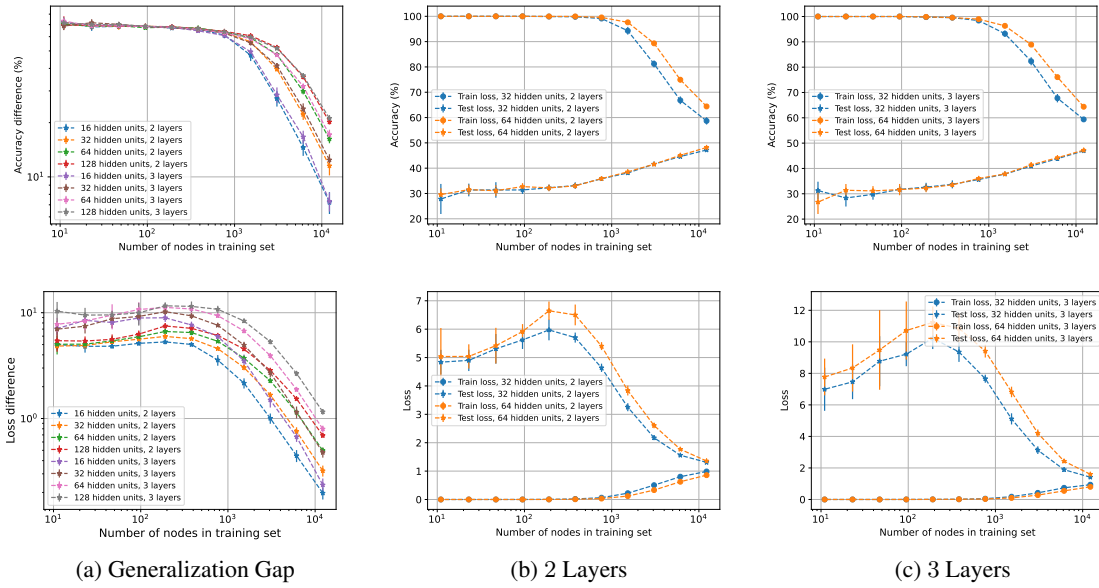


Figure 22: Generalization gap, testing, and training losses with respect to the number of nodes in the Amazon dataset. The top row is in accuracy, and the bottom row is the cross-entropy loss.

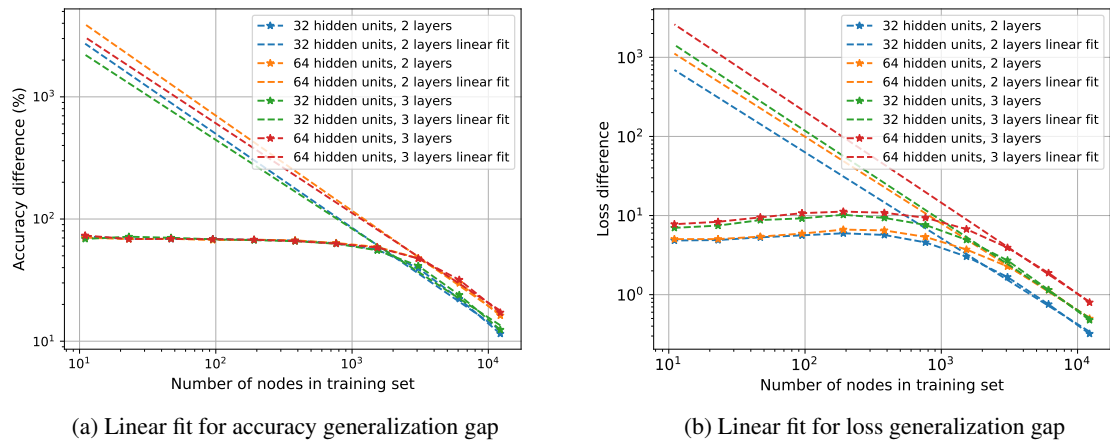


Figure 23: Generalization Gaps as a function of the number of nodes in the training set in the Amazon dataset.

Isomap, implicitly employ low-pass filtering. Therefore, we believe that the low-pass filter assumption is not restrictive and is well-supported by both practical applications and theoretical considerations.

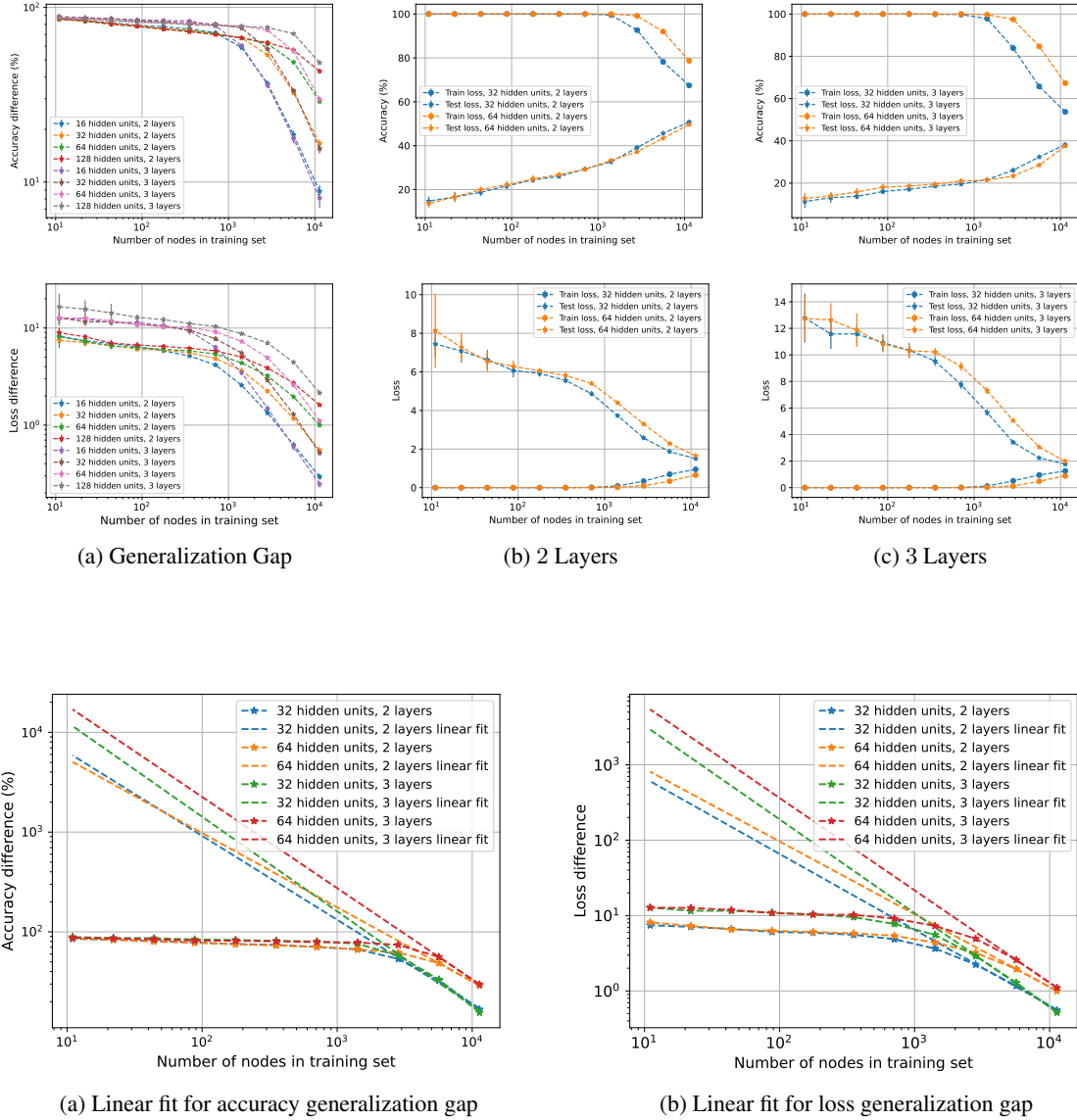


Figure 25: Generalization Gaps as a function of the number of nodes in the training set in the Roman dataset.

Type	Lay.	Feat.	Slope	Point	Pearson Correlation Coefficient
Accuracy	2	32	$-8.408e-01$	$4.644e+00$	$-9.963e-01$
Accuracy	2	64	$-7.435e-01$	$4.477e+00$	$-1.000e+00$
Accuracy	3	32	$-9.476e-01$	$5.049e+00$	$-9.956e-01$
Accuracy	3	64	$-9.145e-01$	$5.182e+00$	$-1.000e+00$
Loss	2	32	$-1.006e+00$	$3.829e+00$	$-9.992e-01$
Loss	2	64	$-9.656e-01$	$3.915e+00$	$-1.000e+00$
Loss	3	32	$-1.244e+00$	$4.764e+00$	$-9.994e-01$
Loss	3	64	$-1.225e+00$	$5.011e+00$	$-1.000e+00$

Table 10: Details of the linear approximation of the Roman Dataset. Note that in this case we used only the values of the generalization gap whose training error is below 95%